RNA Structure Coordinates Translation Across the Meiotic Program

Hao Wu[1,2,*], Caini Zhou[1], Shoucheng Du[1], Simon Felder[2], Yihan Xiong[1], Kevin M. Weeks[2,*] and Yun Bai[1,3,*]

[1]School of Life Science and Technology, ShanghaiTech University, 201210 Shanghai, China
[2]Department of Chemistry, University of North Carolina, Chapel Hill, NC 27599-3290, USA
[3]Deceased
*Correspondence: wuhao@unc.edu (H.W.); weeks@unc.edu (K.M.W.); ybai@shanghaitech.edu.cn (Y.B.)

SUMMARY

mRNA structure is a key determinant of translation efficiency for individual transcripts, yet its role in coordinating complex physiological processes remains elusive. We profiled mRNA structures during yeast meiosis, deriving a high-resolution structurome covering ~70% of annotated mRNAs, with multi-time-point measurements for 2,084 mRNAs. Transcripts upregulated during meiosis generally have flexible structures that enhance translation. In contrast, complex structures impede translation during meiosis by reducing ribosome flux in coding regions and promoting alternative initiation, including in the highly abundant transcript *CCW22*. We uncovered a high-low-high oscillation in cytoplasmic RNA helicase levels, which dynamically reprograms cell-wide translational preferences for RNA structure, shaping the temporal translation of hundreds of mRNAs. Disrupting RNA structure in *CCW22* or altering Ded1p helicase levels interfered with meiotic proteostasis, hindering meiosis progression. Our study reveals that the concerted action of RNA structure and RNA helicases coordinates cell-wide translation dynamics, highlighting a potent post-transcriptional regulatory layer during meiosis when transcription is limited by chromosome condensation.

KEYWORDS

RNA structure, meiosis, translation timing, RNA helicase

INTRODUCTION

RNA molecules adopt elaborate structures that underlie diverse regulatory functions[1]. Advances in high-throughput structure-probing have revealed RNA structural landscapes in diverse entities, from viruses to animals[2–7]. Pioneering studies have advanced our understanding of RNA folding under static conditions and emphasized broad switch-like functions for RNA structure in modulating translation. RNA structures have been evaluated within dynamic cellular contexts, such as isolated cellular compartments[8], different phases of zebrafish embryogenesis[9], and pattern-triggered immunity in *Arabidopsis*[10]. These studies have identified specific structural features and their roles in state-specific gene regulation. Unexplored are general rules for how RNA folding systematically coordinates gene expression during dynamic cellular processes.

RNA structure profoundly impacts translation, a process inherently dependent on mRNA-ribosome interactions. Although the majority of ribosomes, likely over 90% in bacterial cells[11], are actively engaged in translation, a substantial fraction of mRNAs remains untranslated[12]. These observations imply that ribosome resources are scarce relative to mRNAs and emphasize the need for their stringent allocation. Moreover, the proportion of actively translated mRNAs varies across cell types and physiological states[13], raising a critical question: What mechanisms, during dynamic processes, prioritize and alter mRNA access to limited ribosome resources?

Meiosis, a conserved eukaryotic developmental process, has been extensively studied in *Saccharomyces cerevisiae*, providing insights into the multi-layered regulation of stage-specific gene expression. Earlier studies have primarily focused on the cascade of transcription factors[14], yet transcriptional regulation is likely limited when chromosomes are in various stages of movement and condensation, a defining feature of meiosis. Ribosome profiling studies highlight extensive translation control during meiosis[15], involving modulation of RNA-binding protein interactions[16], use of upstream open reading frames (uORFs)[17], and transcript isoform switching[18]. However, the mRNA structural landscape during meiosis remains uncharacterized, leaving the regulatory roles of RNA folding unexplored. The unique attributes of budding yeast, including reduced cellular heterogeneity relative to multicellular organisms, a genome with fewer introns, and established synchronization protocols[19], enable high-resolution determination of RNA structure during this dynamic process.

In this study, we conducted dimethyl sulfate (DMS) mutational profiling (DMS-MaP) and RNA-seq across seven meiotic stages spanning the two nuclear divisions, together with two control states of vegetative growth and pre-meiotic stage. We found that transcripts upregulated during meiosis adopted more flexible structures than those from vegetative growth. RNA structural complexity and translation efficiency (TE) showed stronger correlations during meiosis, with complex structures reducing ribosome flux in coding regions and promoting translation from uORFs. This translational preference for RNA structure displayed an oscillating pattern that delayed translation of structured mRNAs to later stages, particularly for abundant transcripts like *CCW22*. We validated the role of RNA structural elements in governing *CCW22* translation timing using data-directed structure modeling and in-cell reporter systems.

Notably, cytoplasmic mRNA helicases also showed oscillating expression patterns matching the translational preference for RNA structure. Overexpression of Ded1p helicase disrupted the timely translation of transcripts upregulated during meiosis in an RNA structure-dependent manner, causing meiosis progression to pause at metaphase II. Collectively, our work reveals how intrinsic RNA structures and oscillating helicase levels coordinate cell-wide translation timing and meiotic proteostasis. This mechanism is particularly crucial during meiosis, when gene regulation at the transcriptional level is compromised by chromosome condensation and movement, necessitating an additional layer of gene regulation at the post-transcriptional level.

RESULTS

High-resolution DMS-MaP Resolves mRNA Structures Across Yeast Meiosis

To generate comprehensive mRNA structure profiles of the yeast meiotic program, we employed synchronous meiosis to achieve stage-specific resolution and sampled multiple time points for optimal transcriptome coverage. Specifically, meiosis was synchronized by inducing expression of the transcription factor Ndt80p with estrogen[19], and samples were collected across seven meiotic stages, staged by spindle morphology imaging[20] (Fig. S1A): pachytene/pre-induction (T0), end of prophase I (T1), metaphase I (T2), anaphase I (T3), metaphase II (T4), anaphase II (T5), and meiotic exit (T6). In addition, vegetative growth (V) and pre-meiotic (P) samples were included as control stages. All samples were analyzed using mRNA-seq and in-cell DMS-MaP (Fig. 1A).

DMS-MaP measures the chemical accessibility of RNA to DMS, a reagent that preferentially modifies unpaired adenosines and cytidines. We generated a comprehensive DMS-MaP dataset for the *S. cerevisiae* transcriptome, comparable in library size (~180 million reads per stage, Table S1) to datasets obtained in studies of mammalian cells[8,21]. DMS treatment selectively modified adenosine and cytidine residues, as expected (Fig. S1B). We quantified DMS reactivities at single-nucleotide resolution[22]. Assessment of Pearson's r value for DMS reactivities between replicates revealed that a read-depth threshold of 350 was sufficient for reproducible structure modeling (Fig. S1C), which we applied in subsequent analyses. The DMS-MaP data showed excellent agreement with structures of well-characterized RNAs like the 5S rRNA[23] and *GLN1* mRNA[5] (Fig. S1D).

We performed quantitative structural analysis using two approaches. First, we pooled data across all stages to generate high-quality structures for 4,739 of 6,666 annotated yeast mRNAs (Table S2), with a median signal-to-noise ratio of 5.8 (Fig. S1E). Of these, 3,399 had near-complete coverage (>80%), and 1,340 covered more than 200 A/C residues (Fig. S1F). To quantify structural complexity, we calculated the Gini index[5], where higher values indicate more extensive DMS protection, as seen in highly structured RNAs such as rRNAs (Fig. 1B). Structural complexity varied greatly among mRNA species (Fig. 1B). For example, *HAC1* mRNA, previously shown to form extensive intramolecular base-pairings[24,25], had a high Gini index of 0.47 (Fig. 1C), whereas *COX8* mRNA, predicted *in silico* to be largely single-stranded, had a Gini index of 0.24 (Fig. 1D).

We also resolved stage-specific structures for 2,471 mRNAs (Fig. 1E), with 2,084 spanning multiple stages, and 1,799 covering three or more stages (Table S3). The Gini index distribution across stages initially decreased and then increased (Fig. 1F). Specifically, the mean value for all structures per stage decreased from vegetative growth to pachytene (V-P: $P < 10^{-44}$, P-T0: $P < 10^{-107}$) and remained low until metaphase I (T2), before increasing substantially at anaphase I (T2-T3: $P < 10^{-130}$) and then remaining at this level until meiotic exit (T5). This pattern suggests the presence of specific cellular factors or processes that contribute to the reduction of global mRNA structural complexity at meiotic entry.

Transcripts Upregulated During Meiosis Adopt Simpler Folding Than Other mRNAs

Given the complex transcriptional cascade during meiosis[14,26], we asked whether transcriptome remodeling at meiotic entry influences global mRNA structural complexity. We analyzed mRNA-

seq data from the nine stages and performed hierarchical clustering of the 2,620 mRNAs that exhibited at least an eight-fold change in abundance, classifying them as either transcripts upregulated during meiosis (TUMs) or non-TUMs (Fig. 2A). Specifically, 1,078 transcripts, characterized by low vegetative expression but increased expression from pachytene (T0), were categorized as TUMs. The remaining 5520 transcripts, which did not significantly change or were downregulated during meiosis, were labeled as non-TUMs. TUMs can be further sub-categorized as early and late groups based on their peak abundance around meiosis I or meiosis II, respectively (Fig. 2A).

We found that TUMs had significantly lower Gini indices than non-TUMs ($P < 10^{-23}$, Fig. 2B), and no significant Gini differences were noted between early and late subgroups of TUMs ($P = 0.061$, Fig. 2B). Thus, as cells enter meiosis, the downregulation of more structured non-TUMs and the upregulation of less structured TUMs collectively reduce global mRNA structural complexity. The subsequent downregulation of early-group TUMs in later meiotic stages may account for the recovery of global structural complexity (Fig. 1F).

Because GC content of an mRNA can, in principle, influence its RNA structural complexity, we asked whether G–C rich codons contribute to the overall flexible folding of TUMs. Comparison of GC content within open reading frame (ORF) regions revealed no significant difference between TUMs and non-TUMs ($P = 0.4$, Fig. S2A). To further exclude the impact of nucleotide composition on structural quantification, we calculated Gini index using only adenosine reactivities. TUMs retained a significantly higher Gini(A) index, indicating reduced base-pairing of adenosines, independent of G or C nucleotides (Fig. S2B). Together, these results demonstrate that the structural differences between TUMs and non-TUMs are not driven by simple differences in nucleotide composition, but instead reflect intrinsic differences in mRNA folding. Given that RNA structures can impede translation and often require ATP-dependent unwinding, the reduced base-pairing in TUMs may reflect evolutionary selection under nutrient-limiting conditions, potentially facilitating more efficient protein synthesis during meiosis.

Coupled Preference for RNA Structure at Transcription and Translation Levels

A prior ribosome profiling study revealed widespread translation control throughout yeast meiosis[15]. Translation efficiencies (TEs) of certain mRNAs like *SPS1* varied up to 100-fold[15]. Although active translation is known to destabilize mRNA structures within coding regions, the extent of this effect in eukaryotes is unclear. We asked whether the simpler folding of TUMs is shaped by translation regulation. Using matched time courses from ribosome profiling and our structurome datasets (Fig. S2C), we examined RNA structural changes in transcripts with dramatic TE fluctuations, including *ECM8*, *SPO20*, *SPS1*, *CLB3*, and *GIP1*[15]. Surprisingly, DMS reactivities remained highly preserved despite TE variations ranging from 15- to 106-fold (Fig. S2D). Analysis of ORF structural complexity ($Gini_{ORF}$) in 390 transcripts with at least 4-fold TE changes showed no correlation between complexity and TE changes ($r = -0.08$; $P = 0.16$, Fig. S2E). These results suggest that the ORF structures are preserved in highly translated mRNAs, potentially due to rapid RNA refolding after ribosome passage. The refolded structures could hinder subsequent ribosomes, highlighting the potential for ORF structure-mediated translation regulation.

We then investigated how preserved ORF structures influence translation by examining the genome-wide association between TE and $Gini_{ORF}$. Complex ORF structures are postulated to

hinder translation elongation[27]. Consistent with this, we observed modest negative correlations between $Gini_{ORF}$ and TEs across all vegetative and meiotic stages (Spearman's r: -0.32, $P < 10^{-261}$, Fig. S2F). The correlations were notably stronger during meiotic stages when TUMs are fully transcribed (T1-T6, Spearman's r: -0.35 ~ -0.56) compared to stages of vegetative growth to pachytene (V-T0, Spearman's r: -0.21 ~ -0.36, Fig. S2G). The strongest correlation emerged at the end of prophase I (T1, Spearman's r = -0.56), where mRNAs with high Gini indices showed significantly lower TEs (Fig. 2D), suggesting enhanced translational repression of highly structured mRNAs during meiosis. Correspondingly, the correlation between RNA abundance and ribosome profiling weakened significantly during meiotic stages (Fig. S2H), further supporting RNA structure as a dominant regulator of translation during meiosis.

To validate the association between RNA structure and TE, we stratified transcripts with quantified structures into three equal-sized groups based on ORF structural complexity: Simple, Moderate, and Complex (Fig. 2E). Among TUMs, the Simple group (n = 448) contained twice as many transcripts as the Complex group (n = 222), consistent with a general trend toward simpler folding (Fig. 2E). Transcripts in the Simple group exhibited significantly higher TEs at all stages, with this difference more pronounced during meiosis: average TEs for Simple group increased from ~1.4-fold during vegetative growth to more than 2.0-fold during meiosis compared to Complex group (Fig. S2I). Consistent with this trend, TUMs displayed relatively low TEs during vegetative growth but achieved higher TEs during meiosis, particularly at early stages (T2 and T3, Fig. S2J), indicating that the meiotic cellular environment is especially permissive for TUM translation. Together, these results demonstrate that the regulatory impact of RNA structure on translation is substantially amplified during meiosis.

To elucidate the mechanisms underlying the amplified translational divergence, we confirmed that structural differences between the Simple and Complex groups were maintained across the 5′UTR, ORF, and 3′UTR regions, where mRNAs in the Complex group exhibited consistently lower DMS reactivities (Fig. S2K). To assess how local ORF structures influence ribosome movement, we segmented ORFs into 50-nucleotide windows and calculated ribosome flux for each window (Fig. 2F). Ribosome flux declined progressively from the 5′ to the 3′ end (Fig. S2L). We defined the most structured region (window 0) as the window with maximal Gini index, which was significantly higher in the Complex group (Fig. S2M), reflecting more intricate local RNA structures. During vegetative growth, ribosome flux decreased similarly in both groups when comparing upstream (−1) and downstream (+1) windows, with a minimal difference of 1.4%. In contrast, during meiosis, the Complex group exhibited ~10% greater reduction in ribosome flux (Fig. 2F), indicating that local RNA structures impose stronger barriers to ribosome progression during meiosis. Given that translation from upstream open reading frames (uORFs) in yeast occurs predominantly during meiosis[15], we asked whether 5′UTR structure influences uORF translation. Analysis of ribosome footprinting in 5′UTRs revealed that the Complex group exhibited twice the frequency of uORF translation compared to the Simple group (Fig. 2G), suggesting that 5′UTR structure promotes alternative start codon usage and enhances uORF translation, thereby suppressing translation of the downstream main ORF.

Overall, our results reveal a meiotic preference for transcription and translation of mRNAs with flexible folding. To quantify this preference, we scaled RNA abundance and ribosome footprint signals to 100% at each time point and calculated the proportional contributions of transcripts stratified by structural complexity. This analysis uncovered strong coupling among transcriptome

composition, ribosome resource allocation, and RNA structure (Fig. 2H). Notably, both RNA abundance and translation displayed an oscillatory preference for RNA structure. During vegetative growth, mRNAs of differing structural complexity contributed comparably. Upon entering meiosis, however, transcripts with flexible folding became overrepresented and were preferentially engaged by ribosomes, before returning to a more balanced distribution at meiotic exit (Fig. 2H). To further define translational preferences independent of RNA abundance, we normalized the ribosome occupancy by mRNA abundance, revealing a similar oscillation pattern in TE across meiosis (Fig. 2H). These findings demonstrate dynamic coupling between transcriptional output and translational prioritization based on RNA structure, enabling efficient ribosome resource allocation to newly transcribed mRNAs during meiosis.

mRNA Structure Contributes to Stage-Specific Gene Expression

A central question in meiosis is how pre-transcribed mRNAs are selectively translated at distinct stages. Although TUMs generally have simpler structures, their structural complexity still varies considerably (Fig. 3A). We explored whether RNA structure differences among TUMs influence their translational dynamics. We similarly classified TUMs into three equal groups based on Gini indices and compared their ribosome resource occupancy from pachytene (T0). The Simple group peaked in ribosome resource occupancy around anaphase I (T3: 40%), while the Complex group surged only during meiotic exit (T5: 8.7%, T6: 20.5%). The Moderate group had a pattern that fell between these two extremes (Fig. 3A). This pattern is strongly associated with the structural complexity in 5'UTR and ORF regions, but not 3'UTR regions (Fig. S3A). Gene Ontology (GO) analysis revealed stage-specific functional associations: Genes involved in early-stage events such as synapsis, meiotic recombination, and chromosome segregation were predominantly in the Simple and Moderate groups. In contrast, genes in the Complex group were primarily associated with cell wall activities (Fig. S3B and Table S4), which are critical during gamete maturation following the two meiotic divisions. Moreover, genes known for translation delayed until the end of meiosis II[28], such as *SPS1*, *SPS4*, and *SSP2*, were significantly enriched in the Complex group ($P < 10^{-7}$, Table S5). These findings suggest that ribosome resources are dynamically allocated to TUMs in an RNA structure-dependent manner to support their stage-specific functions.

To evaluate the role of RNA structure in meiotic protein dynamics, we conducted quantitative proteomics across four meiotic stages (Table S2): pachytene (T0), metaphase I (T2), anaphase II (T5), and meiotic exit (T6). Among 3,989 quantified proteins, including both TUMs and non-TUMs, 690 changed significantly (>1.2-fold, $P < 0.05$). These proteins clustered into three groups based on their peak abundance: before meiosis, during mid-meiosis, and near meiotic exit (Fig. 3B). Proteins peaking in mid-meiosis had significantly simpler RNA structures compared to the other groups (Fig. 3C), aligning with the oscillatory preference for RNA structure. These results confirmed a connection between mRNA structure and meiotic protein dynamics.

To evaluate the role of RNA structure in translation timing, we classified 1,666 genes with >8-fold changes in ribosome footprints into three groups, similar to those in protein clusters, but based on their translation profiles (Fig. S3C). Significant overlaps in mRNAs clustered by ribosome footprint or protein level at each stage (before, $P < 10^{-38}$; middle, $P < 10^{-50}$; late, $P < 10^{-18}$; Fig. 3D) indicate that translation timing governs meiotic protein dynamics. Consistent with the trend in proteins, highly translated mRNAs exhibited high-low-high oscillation in structural complexity (Fig. S3D). Notably, 217 transcripts with peak translation near meiotic exit, including Ndt80 targets known for

261 delayed translation timing such as *CLB3*[19] and *SPS1*[28], had more complex structures than mRNAs
262 translated during middle meiosis ($P < 10^{-11}$), and were enriched in the Complex group ($P < 10^{-7}$,
263 Table S6). RNA-seq profiles revealed that these genes were transcribed during early stages, from
264 pachytene to metaphase II (Fig. S3E), highlighting varying degrees of translation delays. Gini
265 index comparison revealed that mRNAs with peaked translation near meiotic exit had higher
266 complexities in 5'UTRs and ORF ($P = 0.016$ and $P < 10^{-9}$, respectively), but not 3'UTRs (Fig. 3E
267 and Table S7), suggesting that complex 5'UTR and ORF structures delay translation.
268
269 Given that abundant transcripts impose greater demands on ribosome resources, we analyzed
270 RNA abundance among mRNAs translated during middle and late meiosis and found that highly
271 abundant transcripts exhibit pronounced structural differences associated with translational timing
272 (Fig. 3F). For example, *CCW22*, the most abundant mRNA during meiosis encoding a cell wall
273 protein, was translated near meiotic exit and had an exceptionally high Gini of 0.414 (Fig. 3F).
274 Despite continuous accumulation, *CCW22* mRNA showed relatively high TEs only during
275 vegetative growth and again during late meiotic stages (Fig. 3G). Ribosome footprint analysis
276 revealed increased use of a near-cognate start codon (*AUA*) at position -17 in its 5′UTR
277 specifically during low TE stages (Fig. 3G). This codon resides in a long-range 22 bp interaction
278 spanning the 5′ and 3′UTR, as revealed by DMS-MaP structural modeling (Fig. 3H). The stem
279 harboring the *AUA* codon shows lower pairing probability, suggesting ribosome stalling here may
280 locally disrupt the structure (Fig. 3H). The 5′UTR-3′UTR interactions appear to hinder ribosome
281 progression during specific stages, thereby promoting near-cognate start codon usage.
282
283 To confirm a role for the 5′UTR-3′UTR interactions in regulating *CCW22* translation timing, we
284 truncated either UTR in a reporter construct, which led to earlier Ccw22p expression, compared
285 to the wild-type construct (Fig. S3F). Disrupting the interactions by mutating 3′UTR nucleotides
286 that pair with the 5′UTR similarly resulted in earlier Ccw22p expression (Fig. 3I). Restoring the
287 interactions by mutating the 5′UTR rescued the oscillatory expression (Fig. 3I). All constructs
288 showed rapid mRNA accumulation during early stages (Fig. S3G), but structure-disrupted mRNAs
289 failed to further accumulate at late stages, suggesting that 5'UTR-3'UTR interactions also
290 influence mRNA stability. Despite the greater accumulation of RNA abundance from wild-type and
291 structure-restored constructs, protein synthesis is largely suppressed during early meiotic stages.
292 These results validate that the long-range 5′UTR-3′UTR interactions of *CCW22* modulate its
293 oscillatory translation.
294
295 Consistent with its extreme abundance, ribosome resources occupied by *CCW22* increased from
296 0.05% during pachytene to 4.2% at meiotic exit (Fig. S3H). This pronounced engagement
297 underscores the capacity of structural elements within *CCW22* to influence global translation
298 events. Supporting this model, a yeast strain expressing a *CCW22* variant unable to form 5′UTR-
299 3′UTR interactions showed a significant delay in meiosis progression (Fig. S3I), despite *CCW22*
300 not having been previously implicated in meiosis. Together, these results show that failure to
301 restrain translation of highly abundant transcripts can exert cell-wide effects through competitive
302 access to a finite ribosome pool, underscoring the role of RNA structure in ensuring proper meiotic
303 progression.

304 **mRNA Unwinding Power Oscillates to Coordinate Meiotic Proteostasis**

305 We hypothesized that the dynamic allocation of ribosome resources arises from fluctuations in
306 cellular sensitivity to mRNA structures, or what we term mRNA unwinding power. RNA helicases

have been identified as the primary factors unwinding RNA structures *in vivo*[29]. In mammals, RNA helicases such as YTHDC2, DHX36, and Ddx25 play pivotal roles at various stages of meiosis and spermatogenesis[30–32], suggesting that these factors precisely modulate unwinding power across different developmental stages.

To evaluate mRNA unwinding power across meiosis, we analyzed the expression of 14 cytoplasmic RNA helicases and 2 helicase-regulating accessory proteins. Because our study lacks proteomic quantification of vegetative growth and gamete maturation, we referenced a prior study of SK1 yeast undergoing natural meiosis[18] (Table S8). Co-clustering of helicase expression at the translation and protein levels revealed two distinct patterns (Fig. 4A). One group, including Ded1p, showed a continuous decline from vegetative growth to gamete maturation, while another group, like Dbp1p, showed low levels in early meiosis, followed by an increase in later stages. Overall, mRNA unwinding power oscillates across meiosis, as shown by the high-low-high pattern of total ribosome footprints of these helicase genes (Fig. S4A).

We propose that transcripts respond differentially to oscillating unwinding power based on their intrinsic folding. Under low unwinding power, mRNAs with flexible folding are efficiently translated, whereas those with complex structures are not. Conversely, in a high-unwinding-power state, all mRNAs receive sufficient helicase-mediated unwinding for efficient translation. This model aligns with observed cellular translational preferences: mRNAs with flexible folding are preferentially translated during a low-helicase state at early meiotic stages, while mRNAs with complex folding, such as *CCW22*, are efficiently translated only in a high-helicase state, including vegetative growth and later meiotic stages (Fig. 2H and Fig. 3E).

To test this model, we disrupted meiosis-specific suppression of RNA helicases by overexpressing Ded1p, a helicase known to resolve 5′UTR structures[33]. Both ribosome profiling and proteomic data revealed a 50% decrease in Ded1p levels from vegetative growth (V) to pachytene（T0), which remained at low levels until the end of meiosis (Fig. 4B and Fig. S4B). To elevate Ded1p levels, we used the *CDC5* promoter, identified via GFP reporter assays to drive robust expression during meiosis (Fig. S4C). Quantitative proteomic analysis revealed that Ded1p rose to a near-vegetative level by anaphase II (T5, Fig. 4B) under control of *CDC5* promoter. Given that repressed Ded1p enhances the use of near-cognate translation initiation codons[17], we measured Ccw22p abundance under Ded1p overexpression and observed premature Ccw22p expression starting from early meiosis I (Fig. 4C). This result supports that elevated Ded1p alleviated ribosome stalling and alternative initiation at the near-cognate start codon within the 5′UTR-3′UTR structure (Fig. 3H), thereby releasing its translation.

Disrupted mRNA unwinding power should lead to misallocation of global ribosome resources in an RNA structure-dependent manner, thereby disrupting meiotic proteostasis. To test this prediction, we conducted differential protein expression analysis comparing wild-type and Ded1p-overexpressing conditions. This comparison identified 149 genes upregulated and 194 genes downregulated by at least 1.2-fold under Ded1p overexpression ($P < 0.05$; Fig. 4D and Table S9). Significantly, upregulated genes had more complex mRNA structures than downregulated ones ($P < 10^{-5}$; Fig. S4D). Region-specific comparisons showed that upregulated genes had more structured 5′UTRs ($P = 0.014$, Fig. 4E), consistent with Ded1p's role in unwinding 5′UTR secondary structures. In contrast, downregulated genes showed simpler ORF structures ($P < 10^{-5}$, Fig. 4E), suggesting that their suppression may arise indirectly from ribosome reallocation rather

than direct Ded1p effects. The 3′UTRs of downregulated genes were also less structured than genes with non-significant changes, but the difference was subtler. These findings confirm that elevated helicase levels during meiosis globally skew translation resources toward mRNAs with complex structures.

Because TUMs generally adopt flexible structures favored during low-unwinding-power stages, we evaluated how elevated unwinding power influences TUM expression and meiotic progression. Gene Set Enrichment Analysis (GSEA) revealed a widespread decrease in abundance for TUM-encoded proteins upon Ded1p overexpression (Fig. 4F), with the strongest reductions observed for the most structurally flexible TUMs, including *SPO19*, *SPR1*, and *GAS4* (Gini = 0.28, 0.27, 0.27, respectively). Consistent with these changes, Ded1p overexpression severely disrupted the meiotic cell cycle, frequently causing arrest at or before metaphase II, as revealed by immunofluorescence staging at 12 hours post-induction (Fig. 4G). Together, these results show that fluctuations in mRNA unwinding power orchestrate ribosome resource allocation among mRNAs with differing structural complexities (Fig. 5). This mechanism directs orderly gene expression and is crucial for faithful execution of meiotic program.

Discussion

High-throughput analysis of mRNA structure in eukaryotes requires deep sequencing to capture low-abundance transcripts within complex genomes, and extending such analyses across dynamic biological processes presents an even greater challenge. Most studies to date have focused on a few cell states or individual RNA elements, leaving a gap in our understanding of how RNA structure systematically regulates dynamic cellular processes. Here, we generated a high-resolution mRNA structural map across nine stages of synchronized yeast meiosis, covering approximately 70% of annotated mRNAs. Integrating this dataset with measurements of mRNA abundance, translation, and protein output revealed RNA folding as a broad regulatory program that coordinates selective gene expression across meiotic stages to ensure accurate execution of meiosis (Fig. 5).

Upon entering meiosis, cells transcribe a large cohort of mRNAs (TUMs) whose structures are generally flexible but still exhibit considerable diversity in their folding. During early meiosis, cytoplasmic RNA helicases are globally suppressed, limiting unwinding power and biasing ribosome resources toward mRNAs with flexible structures, including most TUMs. In contrast, highly structured mRNAs encounter translation inhibition, as complex structures reduce ORF ribosome flux and enhance uORF translation (Fig. 2F and Fig. 2G). This disparity in mRNA translatability enables selective expression for newly transcribed TUMs and facilitates rapid translational reprogramming into a meiotic mode. During late meiosis II, upregulation of specific helicases restores mRNA unwinding power, releasing translational repression of structured mRNAs. This mechanism highlights a post-transcriptional regulatory layer embedded in intrinsic mRNA folding potential, which becomes particularly critical when chromosome compaction limits new transcription during meiotic divisions.

Through time-resolved multi-omics clustering at both transcriptional (Fig. 2A and 2B) and translational (Fig. S3C and S3D) levels, we identified general RNA structural features associated with temporal regulation. For example, mRNAs with complex 5′UTR and ORF structures tend to be translated at later stages, enabling coordinated expression of functionally synergistic proteins. Similar structural features have been observed in mRNAs that participate in other environmental response processes, including double-stranded RNA structures downstream of upstream AUGs in immune response genes[10] and structured regions that occur shortly after start codons in autophagy genes[34]. Such findings suggest that shared mRNA structural features serve as a widespread strategy to coordinate synergistic gene expression in response to complex environmental cues.

Beyond identifying functional RNA structures, our study supports a systemic model in which mRNAs compete for a finite pool of ribosome resources based on their intrinsic folding (Fig. 2H and 3A). This zero-sum model emphasizes how translation can be globally coordinated by RNA structure. For example, *CCW22*, a highly abundant transcript, adopts elaborate 5′UTR-3′UTR interactions that prevent monopolization of ribosome resources at inappropriate stages. Critically, ribosome resource allocation is dynamically modulated by RNA helicases in an RNA structure-dependent manner, such that changes in helicase expression mean that mRNA groups with similar structural complexity gain or lose a translational advantage. This framework provides a unified explanation for prior observations, including the effects of Ded1 inactivation on global TEs[35]: Ded1 inactivation suppresses translation of mRNAs with structured 5′UTRs, and

417 simultaneously enhances translation of mRNAs with simple 5′UTRs. Focusing solely on individual
418 transcripts makes it difficult to explain the enhanced translation under helicase inactivation. By
419 contrast, our model attributes this dual effect to a transcriptome-wide reallocation of ribosome
420 resources from highly structured to more flexible mRNAs, a finding supported by our helicase
421 overexpression experiments (Fig. 4D and 4E).
422
423 We observed that mRNA unwinding power oscillates in a high-low-high pattern during meiosis, a
424 combinatorial outcome of the expression dynamics of two classes of cytoplasmic helicases. The
425 mRNA unwinding power described here is an estimate derived from their collective expression
426 patterns. This approximation was used because the roles of many helicases in translation have
427 not been thoroughly studied, and their unwinding activities are influenced by multiple factors such
428 as accessory proteins and RNA-binding proteins[40]. We confirmed that Ded1p suppression is
429 required for preferential translation of TUMs, particularly those with highly flexible structures (Fig.
430 4F). However, the helicases responsible for activating translation of highly structured mRNAs
431 remain to be identified. Proteomic profiling of natural meiosis revealed a coordinated upregulation
432 of several helicases known to be involved in mRNA translation (Fig. 4A). For example, Dbp1p, a
433 'low performance' paralog of Ded1p[36], may substitute in unwinding structured 5′UTRs, while
434 Dhh1p, associated with ORF structure unwinding[34], may facilitate translation of structured ORFs
435 during late meiosis. Although this study focuses on meiosis, fluctuations in helicase expression
436 have been implicated in other physiological and pathological contexts, including innate immune
437 responses, neurodegenerative diseases, and multiple cancers[37]. As shown here for meiosis,
438 helicase-mediated ribosome resource reallocation at the post-transcriptional level may represent
439 a common mechanism that regulates diverse biological processes.

Data availability

The raw sequencing data are available at the NCBI BioProject under accession number PRJNA1174166. Scripts used for sequencing data processing and analysis are accessible at the GitHub repository: https://github.com/HoNg621/StructuromeYeastMeiosis. The mass spectrometry raw data have been deposited in the ProteomeXchange Consortium member repository with accession code PXD056964. Further inquiries regarding resources and reagents should be directed to the lead contact, H.W. (wuhao@unc.edu).

Acknowledgments

This work was supported by the National Key Research and Development Program of China (2016YFA0500900 to Y.B.), start-up funding from ShanghaiTech University (to Y.B.), and the US National Institutes of Health (R35 GM122532 to K.M.W.). We thank the Molecular and Cell Biology Core Facility (ShanghaiTech University), the Molecular Imaging Core Facility (ShanghaiTech University), and the Multi-Omics Core Facility (ShanghaiTech University) for technical support. We are indebted to Yang Yang (ShanghaiTech University) for critical comments. We thank Wei Li (Guangzhou Women and Children's Medical Center) for sharing yeast strains, and Jilong Liu (ShanghaiTech University) for sharing plasmids.

Author contributions

Y.B. conceived of and supervised the study. H.W. and Y.B. designed the experiments with assistance from C.Z. H.W. and Y.B. designed the analyses. H.W. and C.Z. performed the experiments with assistance from S.D. and Y.X. H.W. performed the analyses. H.W., Y.B., and K.M.W. wrote and revised the manuscript with contributions from S.F.

Declaration of interests

The authors declare no competing interests, with the exception that K.M.W. is a founder at ForagR Medicines, Ribometrix and A-Form Solutions.

METHODS

Synchronous meiosis conditions

The yeast strain A14201 (SK1 background), commonly used in meiotic studies, was cultured to saturation in YPD medium (1% yeast extract, 2% peptone, 2% glucose). This culture was then diluted to an optical density at 600 nm (OD_{600}) of 0.3 in YPA medium (1% yeast extract, 2% peptone, 1% potassium acetate, pH = 7.0) and grown overnight. Cells were washed twice and resuspended in SPO medium (0.5% potassium acetate, pH = 7.0, 0.02% raffinose) to an OD_{600} of 1.9. At 6 hours after transfer to SPO, 1 μM β-estradiol was added to induce the meiotic transcription factor Ndt80.

Meiotic staging

Tubulin immunofluorescence was performed to monitor spindle morphology as previously described[20], with minor modifications. Cells were fixed with 3.7% formaldehyde for 20 minutes at room temperature, washed twice with 1x PBS, and resuspended in 100 μl of 1 M sorbitol/PBS. Cell walls were digested with 0.2 U/μl lyticase (Yeasen, 10403ES81) for 20 minutes at 30°C for vegetative cells and 30 minutes at 30°C for sporulating cells. The cells were then adhered to polylysine-treated slides and immersed in -20°C methanol for 6 minutes, followed by 30 seconds in acetone. After air drying, cells were incubated with 5% bovine serum albumin, and the yeast spindle was visualized using primary antibody Mouse anti-alpha-tubulin (Sigma, T5168, 1:1,000) and secondary antibody Cy5-conjugated goat anti-mouse IgG (Jackson ImmunoResearch Laboratories, 115-175-146, 1:200), with DAPI staining for the nuclear region.

DMS-MaP library generation

For *in vivo* modification, 4 ml of yeast cultures (OD_{600} = 0.8 for vegetative) were treated with 200 μl DMS for 4 minutes at 30 °C. Control samples were treated with an equal amount of DMSO. The reaction was quenched with 4 ml of ice-cold stop solution (30% beta-mercaptoethanol), and cells were quickly pelleted and washed with 2 ml stop solution. Total RNA was isolated using a modified hot phenol method suitable for meiotic cells[38] and treated with RNase-free DNase I (Promega, M6101) to remove genomic DNA. Poly(A) mRNA was enriched from 5 μg of total RNA using a Poly(A) mRNA Magnetic Isolation Module (NEB, E7490).

Reverse transcription and second-strand synthesis for mutational profiling were adapted from previous methods[21,39], with modifications to preserve strand information. The first strand was synthesized using SuperScript II (Invitrogen, 18064014) with MaP buffer (50 mM Tris [pH = 8.0], 75 mM KCl, 6 mM $MnCl_2$, 10 mM DTT, 0.5 mM dNTPs) and strand-specific reagent (NEB, E7765). Following G-25 microspin column desalting (GE Healthcare, 27532501), the cDNA was compatible with the second-strand synthesis module in the directional RNA library prep kit (NEB, E7765), which included dUTP incorporation. After purification using SPRIselect beads (NEB, E7765), the double-stranded DNA was enzymatically fragmented using the DNA fragmentation module (NEB, E7810). Most fragments were roughly 400 bp in length. Further library generation procedures, including adaptor ligation, USER enzyme digestion, size selection (> 200bp, 1:1 ratio of beads to sample), and PCR amplification, were performed as per the manufacturer's instructions (NEB, E7765).

505 **Tandem Mass Tag-based LC-MS/MS**

506 For meiotic samples, yeast cultures (2 ml) were spun down and resuspended in 0.7 ml lysis buffer
507 (20 mM HEPES [pH = 7.5], 140 mM KCl, 2 mM EDTA, 1% Triton X-100, 1 × protease inhibitor
508 (APExBIO, K1010)). Cells were then lysed by rigorous vortexing at 4°C with acid-washed glass
509 beads (0.4-mm diameter). Cell debris was removed by centrifugation. The crude proteins were
510 precipitated by adding 10 volumes of cold acetone to the supernatant and kept at -20 °C overnight.
511 The proteins were pelleted by centrifugation and dried with the lid open. The pellet was dissolved
512 in 100 μl urea buffer (8 M Urea, 50 mM NH_4HCO_3).
513
514 To disrupt disulfide bonds, dithiothreitol was added to a final concentration of 5 mM, and samples
515 were incubated for 1 hour at 37 °C in a thermal mixer. Protein concentration was determined using
516 a BCA assay (Yeasen, 20201ES76). Subsequently, 20 mg total protein was then alkylated with
517 10 mM iodoacetamide for 45 minutes at room temperature. Alkylated proteins were diluted 1:8
518 with 50 mM $NaHCO_3$ and digested using trypsin protease (Life/Invitrogen, 90057) for 16 hours
519 with an enzyme-to-substrate ratio of 1:50. The digestion was stopped by the addition of
520 trifluoroacetic acid to a final concentration of 0.4%. The peptides were desalted over C18 columns
521 and eluted in 70% acetonitrile, 0.1% formic acid. Then the samples were evaporated to dryness
522 in a vacuum concentrator and re-dissolved in 50 μl 50 mM tetraethylammonium bromide.
523
524 Peptides were then labeled with 0.2 mg TMT10plex reagent (Thermo Scientific, 90309). The
525 labeling reaction was stopped by adding 1 μl of 5% hydroxylamine. Samples were mixed, desalted
526 over C18 columns, and eluted in 70% acetonitrile, 0.1% formic acid. After drying, the sample was
527 re-dissolved in 500 μl of 50 mM tetraethylammonium bromide. Reverse-phase chromatography
528 was used to reduce peptide complexity; 36 fractions were eluted with gradient elution buffer
529 (increasing concentration of acetonitrile, 0.1% formic acid) and combined into 8 fractions (1-
530 2,10,18,26; 3,11,19,27; 4,12,20,28; 5,13,21,29; 6,14,22,30; 7,15,23,31; 8,16,24,32; 9,17,25,33-
531 36). After evaporation to dryness, liquid chromatography-tandem mass spectrometry (LC-MS/MS)
532 analyses were performed on a Q-Exactive HF-X.

533 **Western blotting assay and RT-qPCR**

534 Protein samples from yeast cultures were prepared and resolved via SDS-PAGE, followed by
535 transfer to polyvinylidene difluoride membranes. Pgk1 and Ccw22-FLAG were detected using
536 primary antibodies Mouse anti-PGK1 (Abcam, ab113687, 1:10,000) and Mouse anti-FLAG
537 (Sigma, F1804-50UG, 1:2,500), respectively. Peroxidase-conjugated goat anti-mouse IgG
538 secondary antibody (Jackson ImmunoResearch Laboratories, 115-035-146, 1:10,000) and ECL
539 luminescent solution (Share-Bio, SB-WB012L) were used for blot detection. For RNA analysis, 2
540 mL samples from corresponding time points were subjected to hot phenol extraction to isolate
541 total RNA, reverse-transcribed (Vazyme, R333-01), and quantified by RT-qPCR (Takara Bio,
542 RR820A) using *ACT1* mRNA as an internal control.

543 **Gene cloning and expression in yeast**

544 The pRS shuttle vector, containing autonomously replicating sequence and centromeric sequence,
545 was used to leverage endogenous replication and chromosome segregation machinery in yeast.
546 This vector also incorporates the G418 resistance gene (KanMX) for selecting positive colonies.
547 Vectors were introduced into yeast cells by electroporation.

548
549 For *CCW22* structure disruption, the *CCW22* ORF plus 1,000 nucleotides upstream of the start
550 codon, containing its endogenous promoter, was cloned into the pRS vector as a wild-type control.
551 Mutations that either disrupted or restored the *CCW22* structure were introduced based on the
552 wild-type vector. G418-resistant clones were induced to undergo meiosis. Yeast culture (2 ml)
553 was collected for protein extraction and Western blot analysis.
554
555 For meiosis-specific overexpression of Ded1p, we initially assessed the promoters (1,000 bp
556 sequence upstream start codon) of 10 candidate genes using a GFP reporter system, identified
557 by RNA-Seq and protein expression profiles. Yeast cultures (200 μL) from the same batch were
558 sampled at various stages during meiosis, fixed with 3.7% formaldehyde, and the GFP
559 fluorescence intensity was measured using a microplate reader. Among the candidates, the *CDC5*
560 promoter showed the most consistent increase in GFP intensity post-Ndt80 induction (Fig. S4B)
561 and was used for Ded1p overexpression. The coding region sequence of *DED1* was cloned into
562 the pRS shuttle vector under the control of the *CDC5* promoter. This vector was introduced into
563 yeast cells to assess the effects of Ded1 overexpression.

564 **DMS-MaP data processing**

565 The SK1 genome sequence and annotation were sourced from a previously published dataset[15].
566 Adaptor sequences were removed using cutadapt[40], and rRNA reads were depleted using a
567 bowtie2-based alignment[41] against rDNA sequences. For mRNA abundance quantification,
568 DMSO library reads were mapped to the SK1 genome using STAR aligner[42], with assigned reads
569 counted to each gene in a strand-specific manner using featureCounts[43]. Finally, read counts
570 were normalized by a TPM (transcripts per million) method.
571
572 For DMS-MaP, antisense reads were removed by another bowtie2-based alignment against the
573 assembled transcriptome. The mutation counts and sequencing depth at single nucleotide
574 resolution were parsed by ShapeMapper2[22] using filtered fastq files as input. For stage-specific
575 DMS reactivity, data from two replicates were merged to calculate the mutation rate, which was
576 further normalized per transcript by the mean mutation rate of the 90-95% most reactive bases.
577 For overall structures, DMS reactivity was calculated in a similar manner, but by pooling data from
578 all stages.

579 **Protein mass spectrometry data processing**

580 Raw mass spectrometry data were quantified using MaxQuant[44] against the yeast proteome
581 reference from UniProt (strain ATCC 204508 / S288c). The false discovery rate (FDR) was set at
582 1% at both the peptide and protein levels. Only proteins identified with at least one 'unique/razor
583 peptide' in all samples were used for subsequent normalization. Total TMT intensity in each
584 sample was scaled to 10^6 (total normalization) following previous studies[18].

585 **ORF ribosome flux and uORF ribosome footprint analysis**

586 To quantify ribosome flux across ORFs, we divided each coding region into 50-nucleotide
587 windows, starting from the 30th nucleotide downstream of the start codon and ending 30
588 nucleotides upstream of the stop codon. Ribosome footprint (A-site) counts were summed within
589 each window, and the Gini index was calculated for windows containing more than 20 adenosine

or cytosine nucleotides. The window with the highest Gini index was defined as position 0, and ribosome flux was evaluated in the immediately adjacent upstream (–1) and downstream (+1) windows.
For uORF analysis, ribosome footprints (A-site) within the –100 to +900 nucleotide region relative to the annotated start codon were normalized to a total of 1000 counts per transcript.

RNA secondary structure modeling

DMS reactivities for adenine and cytosine with sequencing depths over 350 in both DMS-treated and DMSO-treated samples were used for structural modeling. The consensus structure model and base-pairing probabilities were predicted using SuperFold[4], considering long-range interactions (maxPairingDist = 1000). Structural models were visualized with vaRNA[45], and base-pair probabilities were plotted using R4RNA[46].

Meta-gene analysis

The average DMS reactivity was calculated for adenine and cytosine with sequencing depths over 350, based on their relative positions to the first nucleotide of the start codon or the last nucleotide of the stop codon.

Hierarchical clustering

For RNA-Seq and ribosome profiling data, genes showing more than an 8-fold change ($P < 0.05$) in RNA abundance or ribosome footprint across all time points are log-transformed and used for subsequent clustering analysis. For quantitative proteomics data, genes showing more than 1.2-fold change ($P < 0.05$) across 4 sampled time points are used for clustering analysis. For co-hierarchical clustering of RNA helicase levels at the translation and protein levels, ribosome footprint and mass spectrometry data were first z-scored and then combined for clustering analysis. Hierarchical clustering was performed using Cluster 3.0[47] with average clustering based on uncentered Pearson correlation. Clustering data were visualized using Java Treeview[48].

Differential gene expression analysis and function analysis

Fold changes in protein abundance and p-values were calculated using edgeR[49]. Proteins with a fold change over 1.2 ($P < 0.05$) were defined as differentially expressed genes. Gene Ontology enrichment analysis was conducted using g:Profiler[50]. Gene Set Enrichment Analysis was performed using GSEApy[51], with ranked protein expression from a predefined TUMs gene set as input.

Statistics and reproducibility

Unless specified, statistical tests were performed using the Scipy v.1.13 package in Python. Correlation analyses between Gini index and translation efficiency employed Spearman's rank correlation. Comparisons of Spearman's correlation coefficient between stages (Fig. 2D) were performed using the independent samples t-test. Comparisons between Gini indices were performed using the Mann-Whitney U test. Gene overlap analyses between clusters (Fig. 3D) were performed using the hypergeometric test. Statistical significance is denoted by asterisks reflecting the p-values (*P < 0.05, **P < 0.01, ***P < 0.001, ****P < 0.0001; NS, not significant).

628 Multiple testing corrections were applied using the False Discovery Rate (FDR) method to adjust
629 p-values. The number of data points for each analysis is indicated in the figure legends. Unless
630 specified, sequencing and mass spectrometry experiments were repeated twice, and other
631 experiments were repeated at least three times with consistent results.

632 # Reference

633 1. Dolgin, E. (2015). The Elaborate Architecture of RNA. Nature *523*, 398–399.
634 https://doi.org/10.1038/523398a.

635 2. Watts, J.M., Dang, K.K., Gorelick, R.J., Leonard, C.W., Bess Jr, J.W., Swanstrom, R., Burch,
636 C.L., and Weeks, K.M. (2009). Architecture and secondary structure of an entire HIV-1 RNA
637 genome. Nature *460*, 711–716. https://doi.org/10.1038/nature08237.

638 3. Burkhardt, D.H., Rouskin, S., Zhang, Y., Li, G.-W., Weissman, J.S., and Gross, C.A. (2017).
639 Operon mRNAs are organized into ORF-centric structures that predict translation efficiency.
640 eLife *6*, e22037. https://doi.org/10.7554/eLife.22037.

641 4. Mustoe, A.M., Busan, S., Rice, G.M., Hajdin, C.E., Peterson, B.K., Ruda, V.M., Kubica, N.,
642 Nutiu, R., Baryza, J.L., and Weeks, K.M. (2018). Pervasive Regulatory Functions of mRNA
643 Structure Revealed by High-Resolution SHAPE Probing. Cell *173*, 181-195.e18.
644 https://doi.org/10.1016/j.cell.2018.02.034.

645 5. Rouskin, S., Zubradt, M., Washietl, S., Kellis, M., and Weissman, J.S. (2014). Genome-wide
646 probing of RNA structure reveals active unfolding of mRNA structures in vivo. Nature *505*,
647 701–705. https://doi.org/10.1038/nature12894.

648 6. Ding, Y., Tang, Y., Kwok, C.K., Zhang, Y., Bevilacqua, P.C., and Assmann, S.M. (2014). In
649 vivo genome-wide profiling of RNA secondary structure reveals novel regulatory features.
650 Nature *505*, 696–700. https://doi.org/10.1038/nature12756.

651 7. Wan, Y., Qu, K., Zhang, Q.C., Flynn, R.A., Manor, O., Ouyang, Z., Zhang, J., Spitale, R.C.,
652 Snyder, M.P., Segal, E., et al. (2014). Landscape and variation of RNA secondary structure
653 across the human transcriptome. Nature *505*, 706–709. https://doi.org/10.1038/nature12946.

654 8. Sun, L., Fazal, F.M., Li, P., Broughton, J.P., Lee, B., Tang, L., Huang, W., Kool, E.T., Chang,
655 H.Y., and Zhang, Q.C. (2019). RNA structure maps across mammalian cellular compartments.
656 Nat Struct Mol Biol *26*, 322–330. https://doi.org/10.1038/s41594-019-0200-7.

657 9. Beaudoin, J.-D., Novoa, E.M., Vejnar, C.E., Yartseva, V., Takacs, C.M., Kellis, M., and
658 Giraldez, A.J. (2018). Analyses of mRNA structure dynamics identify embryonic gene
659 regulatory programs. Nat Struct Mol Biol *25*, 677–686. https://doi.org/10.1038/s41594-018-
660 0091-z.

661 10. Xiang, Y., Huang, W., Tan, L., Chen, T., He, Y., Irving, P.S., Weeks, K.M., Zhang, Q.C., and
662 Dong, X. (2023). Pervasive downstream RNA hairpins dynamically dictate start-codon
663 selection. Nature *621*, 423–430. https://doi.org/10.1038/s41586-023-06500-y.

664 11. Metelev, M., Lundin, E., Volkov, I.L., Gynnå, A.H., Elf, J., and Johansson, M. (2022). Direct
665 measurements of mRNA translation kinetics in living cells. Nat Commun *13*, 1852.
666 https://doi.org/10.1038/s41467-022-29515-x.

667 12. Halstead, J.M., Lionnet, T., Wilbertz, J.H., Wippich, F., Ephrussi, A., Singer, R.H., and Chao,
668 J.A. (2015). An RNA biosensor for imaging the first round of translation from single cells to
669 living animals. Science *347*, 1367–1671. https://doi.org/10.1126/science.aaa3380.

670 13. Wu, B., Eliscovich, C., Yoon, Y.J., and Singer, R.H. (2016). Translation dynamics of single
671 mRNAs in live cells and neurons. Science *352*, 1430–1435.
672 https://doi.org/10.1126/science.aaf1084.

673 14. Chu, S., DeRisi, J., Eisen, M., Mulholland, J., Botstein, D., Brown, P.O., and Herskowitz, I.
674 (1998). The Transcriptional Program of Sporulation in Budding Yeast. Science *282*, 699–705.
675 https://doi.org/10.1126/science.282.5389.699.

676 15. Brar, G.A., Yassour, M., Friedman, N., Regev, A., Ingolia, N.T., and Weissman, J.S. (2012).
677 High-Resolution View of the Yeast Meiotic Program Revealed by Ribosome Profiling. Science
678 *335*, 552–557. https://doi.org/10.1126/science.1215110.

679 16. Berchowitz, L.E., Kabachinski, G., Walker, M.R., Carlile, T.M., Gilbert, W.V., Schwartz, T.U.,
680 and Amon, A. (2015). Regulated Formation of an Amyloid-like Translational Repressor
681 Governs Gametogenesis. Cell *163*, 406–418. https://doi.org/10.1016/j.cell.2015.08.060.

682 17. Guenther, U.-P., Weinberg, D.E., Zubradt, M.M., Tedeschi, F.A., Stawicki, B.N., Zagore, L.L.,
683 Brar, G.A., Licatalosi, D.D., Bartel, D.P., Weissman, J.S., et al. (2018). The helicase Ded1p
684 controls use of near-cognate translation initiation codons in 5′UTRs. Nature *559*, 130–134.
685 https://doi.org/10.1038/s41586-018-0258-0.

686 18. Cheng, Z., Otto, G.M., Powers, E.N., Keskin, A., Mertins, P., Carr, S.A., Jovanovic, M., and
687 Brar, G.A. (2018). Pervasive, Coordinated Protein-Level Changes Driven by Transcript Isoform
688 Switching during Meiosis. Cell *172*, 910-923.e16. https://doi.org/10.1016/j.cell.2018.01.035.

689 19. Carlile, T.M., and Amon, A. (2008). Meiosis I Is Established through Division-Specific
690 Translational Control of a Cyclin. Cell *133*, 280–291. https://doi.org/10.1016/j.cell.2008.02.032.

691 20. Keeling, J.W.P., and Miller, R.K. (2011). Indirect Immunofluorescence for Monitoring Spindle
692 Assembly and Disassembly in Yeast. In Cell Cycle Checkpoints: Methods and Protocols
693 Methods in Molecular Biology., W. X. Li, ed. (Humana Press), pp. 231–244.
694 https://doi.org/10.1007/978-1-61779-273-1_17.

695 21. Zubradt, M., Gupta, P., Persad, S., Lambowitz, A.M., Weissman, J.S., and Rouskin, S. (2017).
696 DMS-MaPseq for genome-wide or targeted RNA structure probing in vivo. Nat Methods *14*,
697 75–82. https://doi.org/10.1038/nmeth.4057.

698 22. Busan, S., and Weeks, K.M. (2018). Accurate detection of chemical modifications in RNA by
699 mutational profiling (MaP) with ShapeMapper 2. RNA *24*, 143–148.
700 https://doi.org/10.1261/rna.061945.117.

701 23. Madru, C., Lebaron, S., Blaud, M., Delbos, L., Pipoli, J., Pasmant, E., Réty, S., and Leulliot, N.
702 (2015). Chaperoning 5S RNA assembly. Genes Dev. *29*, 1432–1446.
703 https://doi.org/10.1101/gad.260349.115.

24. Rüegsegger, U., Leber, J.H., and Walter, P. (2001). Block of HAC1 mRNA Translation by Long-Range Base Pairing Is Released by Cytoplasmic Splicing upon Induction of the Unfolded Protein Response. Cell *107*, 103–114. https://doi.org/10.1016/S0092-8674(01)00505-0.

25. Aragón, T., van Anken, E., Pincus, D., Serafimova, I.M., Korennykh, A.V., Rubio, C.A., and Walter, P. (2009). Messenger RNA targeting to endoplasmic reticulum stress signalling sites. Nature *457*, 736–740. https://doi.org/10.1038/nature07641.

26. Chu, S., and Herskowitz, I. (1998). Gametogenesis in Yeast Is Regulated by a Transcriptional Cascade Dependent on Ndt80. Molecular Cell *1*, 685–696. https://doi.org/10.1016/S1097-2765(00)80068-4.

27. Bao, C., Loerch, S., Ling, C., Korostelev, A.A., Grigorieff, N., and Ermolenko, D.N. (2020). mRNA stem-loops can pause the ribosome by hindering A-site tRNA binding. eLife *9*, e55799. https://doi.org/10.7554/eLife.55799.

28. Jin, L., Zhang, K., Xu, Y., Sternglanz, R., and Neiman, A.M. (2015). Sequestration of mRNAs Modulates the Timing of Translation during Meiosis in Budding Yeast. Mol Cell Biol *35*, 3448–3458. https://doi.org/10.1128/MCB.00189-15.

29. Bleichert, F., and Baserga, S.J. (2007). The Long Unwinding Road of RNA Helicases. Molecular Cell *27*, 339–352. https://doi.org/10.1016/j.molcel.2007.07.014.

30. Li, L., Krasnykov, K., Homolka, D., Gos, P., Mendel, M., Fish, R.J., Pandey, R.R., and Pillai, R.S. (2022). The XRN1-regulated RNA helicase activity of YTHDC2 ensures mouse fertility independently of m6A recognition. Molecular Cell *82*, 1678-1690.e12. https://doi.org/10.1016/j.molcel.2022.02.034.

31. Zhang, K., Zhang, T., Zhang, Y., Yuan, J., Tang, X., Zhang, C., Yin, Q., Zhang, Y., and Tong, M.-H. (2023). DNA/RNA helicase DHX36 is required for late stages of spermatogenesis. Journal of Molecular Cell Biology *14*, mjac069. https://doi.org/10.1093/jmcb/mjac069.

32. Tsai-Morris, C.-H., Sheng, Y., Lee, E., Lei, K.-J., and Dufau, M.L. (2004). Gonadotropin-regulated testicular RNA helicase (GRTH/Ddx25) is essential for spermatid development and completion of spermatogenesis. Proceedings of the National Academy of Sciences *101*, 6373–6378. https://doi.org/10.1073/pnas.0401855101.

33. Gupta, N., Lorsch, J.R., and Hinnebusch, A.G. (2018). Yeast Ded1 promotes 48S translation pre-initiation complex assembly in an mRNA-specific and eIF4F-dependent manner. Elife *7*, e38892. https://doi.org/10.7554/eLife.38892.

34. Liu, X., Yao, Z., Jin, M., Namkoong, S., Yin, Z., Lee, J.H., and Klionsky, D.J. (2019). Dhh1 promotes autophagy-related protein translation during nitrogen starvation. PLoS Biol *17*, e3000219. https://doi.org/10.1371/journal.pbio.3000219.

35. Sen, N.D., Zhou, F., Ingolia, N.T., and Hinnebusch, A.G. (2015). Genome-wide analysis of translational efficiency reveals distinct but overlapping functions of yeast DEAD-box RNA helicases Ded1 and eIF4A. Genome Res *25*, 1196–1205. https://doi.org/10.1101/gr.191601.115.

742 36. Powers, E.N., Kuwayama, N., Sousa, C., Reynaud, K., Jovanovic, M., Ingolia, N.T., and Brar,
743 G.A. (2024). Dbp1 is a low performance paralog of RNA helicase Ded1 that drives impaired
744 translation and heat stress response. bioRxiv, 2024.01.12.575095.
745 https://doi.org/10.1101/2024.01.12.575095.

746 37. Bohnsack, K.E., Yi, S., Venus, S., Jankowsky, E., and Bohnsack, M.T. (2023). Cellular
747 functions of eukaryotic RNA helicases and their links to human diseases. Nat Rev Mol Cell Biol
748 *24*, 749–769. https://doi.org/10.1038/s41580-023-00628-5.

749 38. Ares, M. (2012). Isolation of total RNA from yeast cell cultures. Cold Spring Harb Protoc *2012*,
750 1082–1086. https://doi.org/10.1101/pdb.prot071456.

751 39. Smola, M.J., Rice, G.M., Busan, S., Siegfried, N.A., and Weeks, K.M. (2015). Selective 2′-
752 hydroxyl acylation analyzed by primer extension and mutational profiling (SHAPE-MaP) for
753 direct, versatile and accurate RNA structure analysis. Nat Protoc *10*, 1643–1669.
754 https://doi.org/10.1038/nprot.2015.103.

755 40. Martin, M. (2011). Cutadapt removes adapter sequences from high-throughput sequencing
756 reads. EMBnet.journal *17*, 10–12. https://doi.org/10.14806/ej.17.1.200.

757 41. Langmead, B., and Salzberg, S.L. (2012). Fast gapped-read alignment with Bowtie 2. Nat
758 Methods *9*, 357–359. https://doi.org/10.1038/nmeth.1923.

759 42. Dobin, A., Davis, C.A., Schlesinger, F., Drenkow, J., Zaleski, C., Jha, S., Batut, P., Chaisson,
760 M., and Gingeras, T.R. (2013). STAR: ultrafast universal RNA-seq aligner. Bioinformatics *29*,
761 15–21. https://doi.org/10.1093/bioinformatics/bts635.

762 43. Liao, Y., Smyth, G.K., and Shi, W. (2014). featureCounts: an efficient general purpose program
763 for assigning sequence reads to genomic features. Bioinformatics *30*, 923–930.
764 https://doi.org/10.1093/bioinformatics/btt656.

765 44. Tyanova, S., Temu, T., and Cox, J. (2016). The MaxQuant computational platform for mass
766 spectrometry-based shotgun proteomics. Nat Protoc *11*, 2301–2319.
767 https://doi.org/10.1038/nprot.2016.136.

768 45. Darty, K., Denise, A., and Ponty, Y. (2009). VARNA: Interactive drawing and editing of the
769 RNA secondary structure. Bioinformatics *25*, 1974–1975.
770 https://doi.org/10.1093/bioinformatics/btp250.

771 46. Lai, D., Proctor, J.R., Zhu, J.Y.A., and Meyer, I.M. (2012). R-CHIE: a web server and R
772 package for visualizing RNA secondary structures. Nucleic Acids Res *40*, e95.
773 https://doi.org/10.1093/nar/gks241.

774 47. de Hoon, M.J.L., Imoto, S., Nolan, J., and Miyano, S. (2004). Open source clustering software.
775 Bioinformatics *20*, 1453–1454. https://doi.org/10.1093/bioinformatics/bth078.

776 48. Saldanha, A.J. (2004). Java Treeview--extensible visualization of microarray data.
777 Bioinformatics *20*, 3246–3248. https://doi.org/10.1093/bioinformatics/bth349.

49. Robinson, M.D., McCarthy, D.J., and Smyth, G.K. (2010). edgeR: a Bioconductor package for differential expression analysis of digital gene expression data. Bioinformatics *26*, 139–140. https://doi.org/10.1093/bioinformatics/btp616.

50. Reimand, J., Kull, M., Peterson, H., Hansen, J., and Vilo, J. (2007). g:Profiler—a web-based toolset for functional profiling of gene lists from large-scale experiments. Nucleic Acids Res *35*, W193–W200. https://doi.org/10.1093/nar/gkm226.

51. Fang, Z., Liu, X., and Peltz, G. (2023). GSEApy: a comprehensive package for performing gene set enrichment analysis in Python. Bioinformatics *39*, btac757. https://doi.org/10.1093/bioinformatics/btac757.

MAIN FIGURE TITLES AND LEGENDS

Figure 1. High-resolution mRNA structurome during yeast meiosis

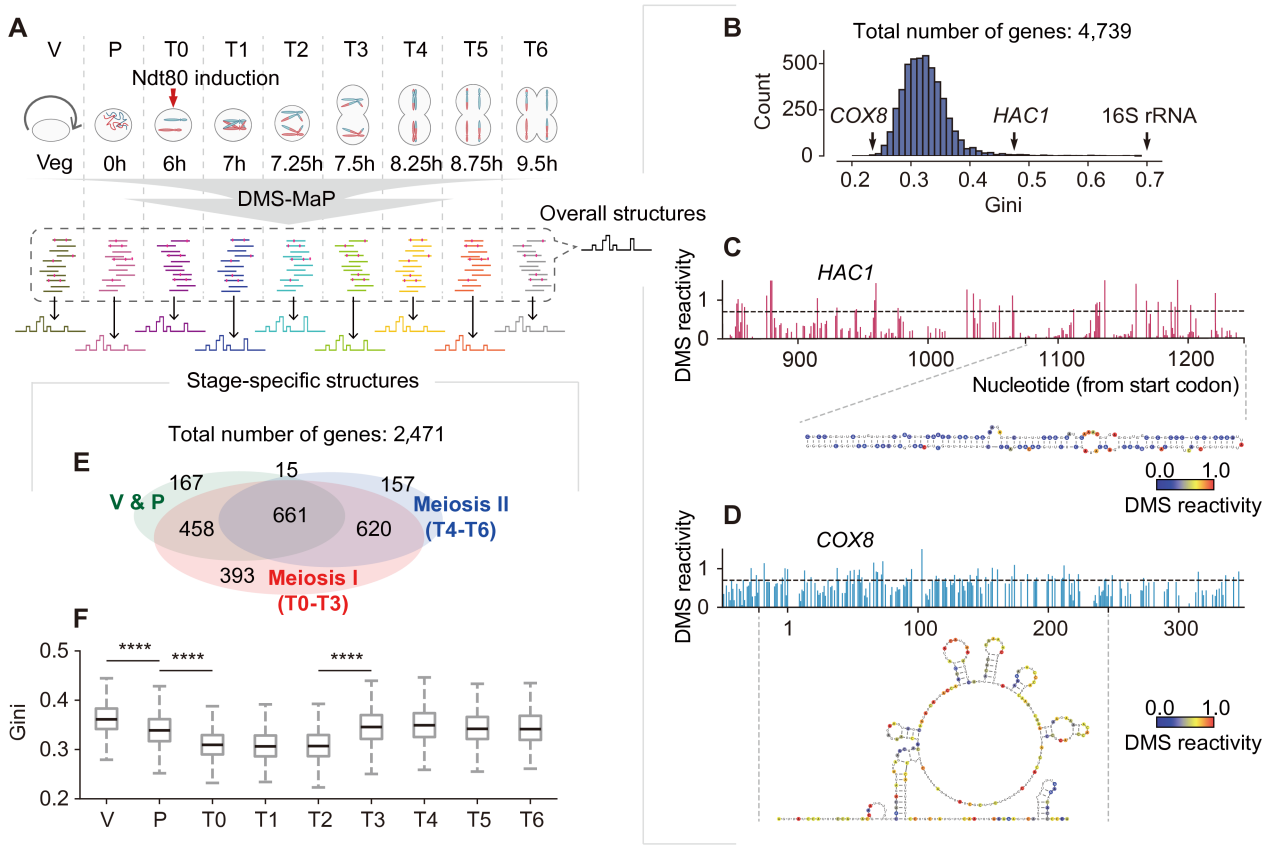

(A) Experimental strategy to obtain mRNA structural maps during yeast meiosis.
(B) Gini index distribution of mRNA structures from 4,739 genes.
(C) DMS reactivities of a 400-nt region in *HAC1* mRNA and corresponding structure model.
(D) DMS reactivities of a 400-nt region in *COX8* mRNA and corresponding structure model.
(E) Venn diagram of the numbers and relationships of stage-specific structures resolved during three periods: vegetative to pre-induction (V-P), early meiosis (T0-T3), and late meiosis (T4-T6).
(F) Gini index distribution of stage-specific structures along the meiosis progression, with statistical significance noted for transitions between stages: V-P, $P < 10^{-44}$. P-T0, $P < 10^{-107}$. T2-T3, $P < 10^{-130}$.

Figure 2. Meiotic preference for transcribing and translating mRNAs with flexible folding

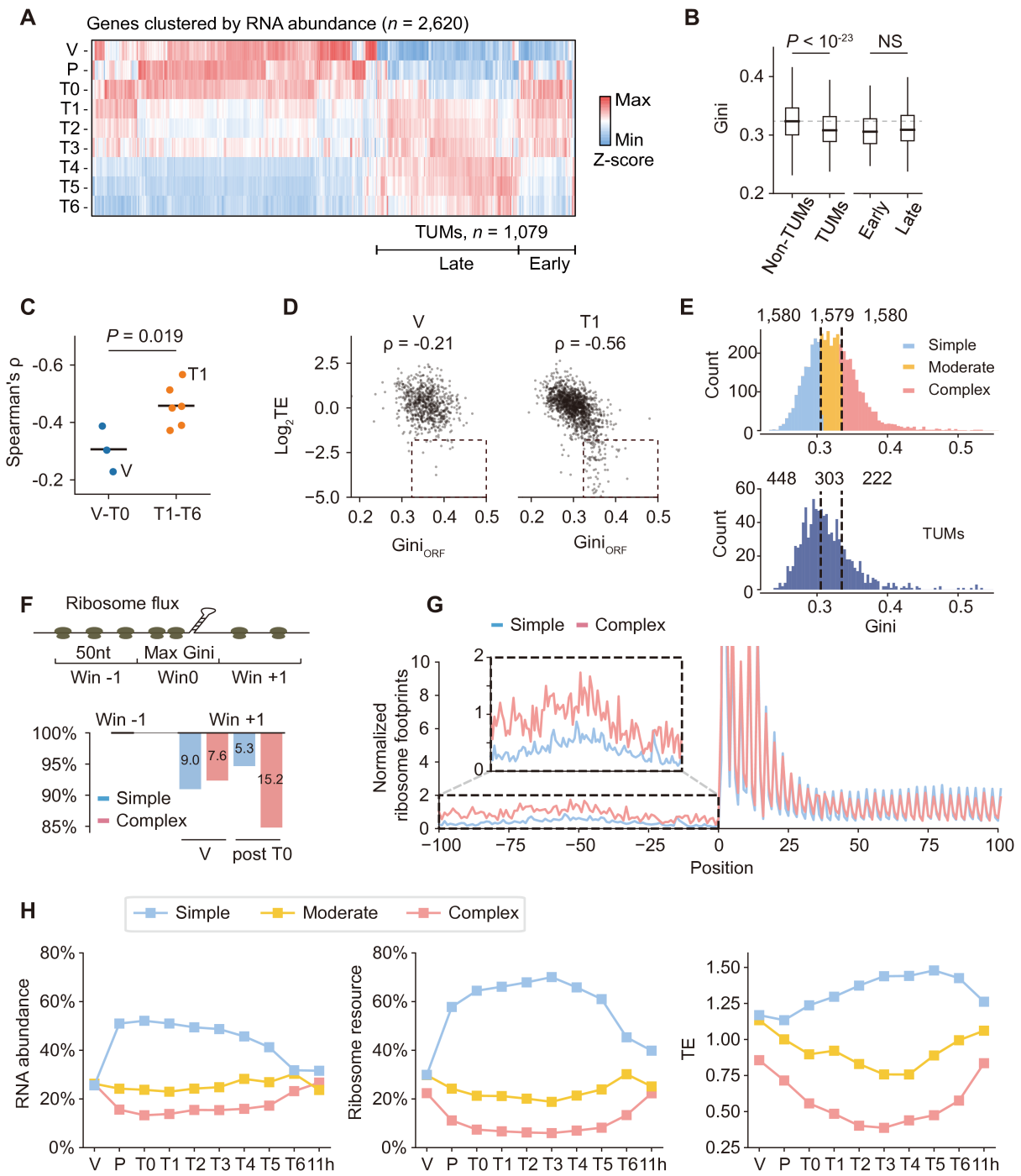

(A) Hierarchical clustering of RNA abundances for genes (n = 2,620) with more than an 8-fold change (P < 0.05) in transcripts per million (TPM) during meiosis.

(B) Distribution of Gini indices in mRNA groups: non-TUMs (n = 3,767), TUMs (n = 937), Early TUMs (n = 251), and Late TUMs (n = 705). The dashed line indicates the median Gini index for the non-TUMs group.

(C) Spearman's rank correlation coefficients between Gini indices and TEs during V-T0 and T1-T6 periods.

811 (D) Relationship between Gini indices and TEs at stage V (with the lowest correlation, n = 736)
812 and stage T1 (with the highest correlation, n = 1,480).
813 (E) Three mRNA groups were classified based on RNA structural complexity: Simple, Moderate,
814 and Complex. The number of TUMs within each group is also indicated with corresponding cutoffs.
815 (F) ORF ribosome flux analysis. Ribosome flux was defined as the sum of ribosome footprint
816 reads (A site) within each 50-nt window. The window with the maximal Gini index was designated
817 as window 0. Ribosome flux in the upstream window (-1) was used for scaling (to 100%) for
818 comparison.
819 (G) Ribosome footprints on uORFs. For each gene, ribosome footprints (A site) from -100 to +900
820 positions relative to the start codon were normalized to a total of 1,000. For each group, the
821 distribution of ribosome footprints was averaged by position.
822 (H) Proportional contribution of mRNA abundance and ribosome footprints. RNA abundance was
823 scaled to 100% to measure the proportion for each group. Similarly, ribosome footprints were
824 normalized to indicate the ribosome resource occupancy for each group. The overall translation
825 efficiency for each group was measured by normalizing ribosome resource occupancy to mRNA
826 abundance proportion.

Figure 3. mRNA structure differences regulate translation timing

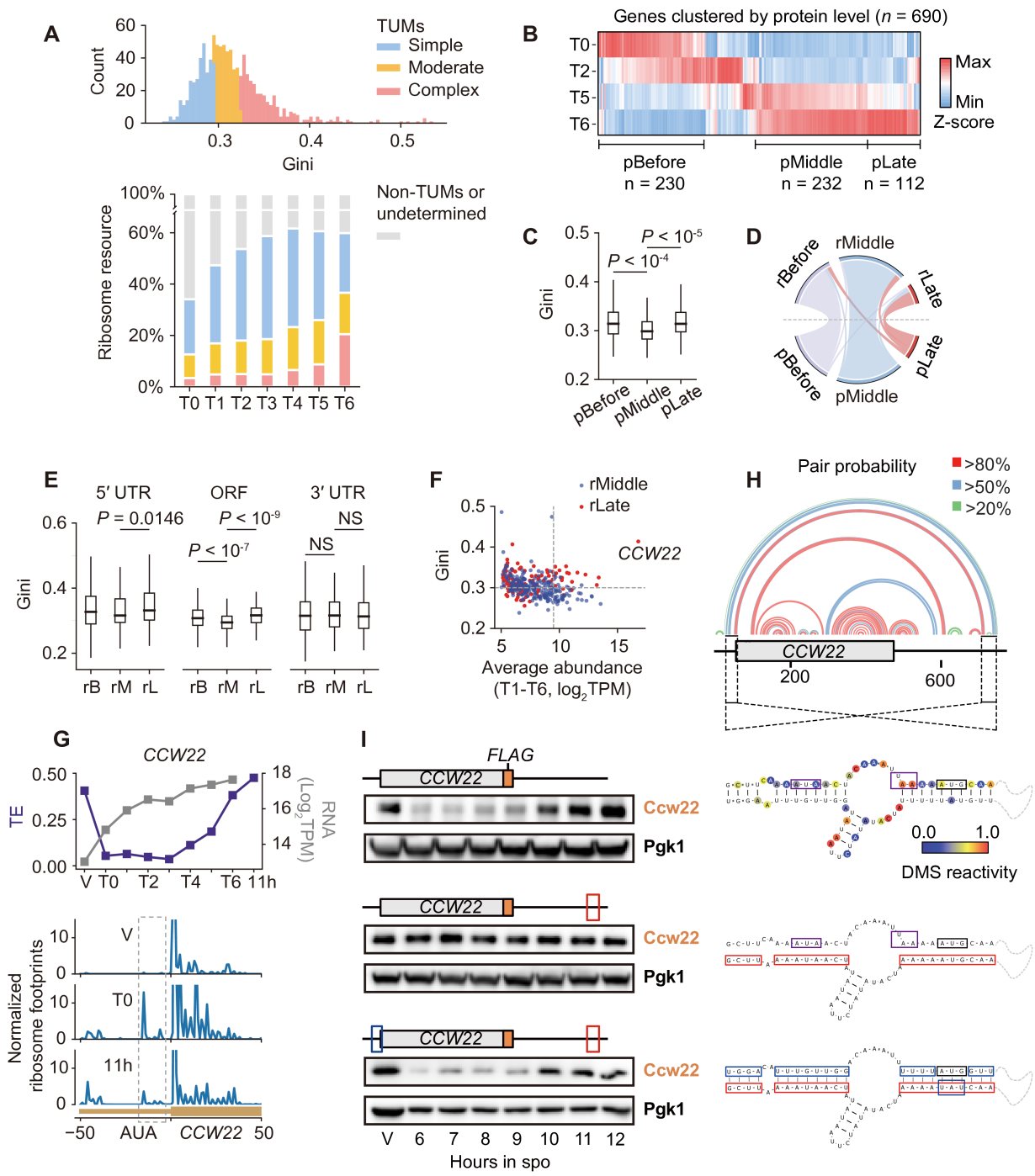

(A) Distribution of Gini indices for TUMs (upper) and dynamic ribosome resource allocation (lower) for three mRNA groups classified based on structural complexity: Simple (n = 324), Moderate (n = 325), and Complex (n = 324).

(B) Hierarchical clustering of protein abundances for genes exhibiting more than 1.2-fold changes (n = 690, $P < 0.05$).

(C) Comparison of Gini indices among three protein groups: before meiosis (pBefore, n = 192), during mid-meiosis (pMiddle, n = 223), and near meiotic exit (pLate, n = 104).

(D) Overlap analysis between genes in ribosome profiling and protein clusters: Before, $P < 10^{-38}$; Middle, $P < 10^{-50}$; Late, $P < 10^{-18}$.

(E) Comparison of Gini indices among ribosomal profiling clusters (rB, rBefore; rM, rMiddle; rL, rLate) across the 5′UTR (rB, n = 331; rM, n = 184; rL, n = 121), ORF (rB, n = 930; rM, n = 268; rL,

840 *n* = 188), and 3′UTR (rB, *n* = 751; rM, *n* = 227; rL, *n* = 143). Only UTRs with coverage of more
841 than 20 A/C were included. Note that the smaller sample size in the 5′UTR contributes to a larger
842 p-value compared to the ORF, which does not necessarily indicate a weaker regulatory effect.
843 (F) Relationship between Gini indices and average mRNA abundance (log_2TPM) during meiotic
844 stages T1-T6.
845 (G) *CCW22* RNA abundance and TE changes during meiosis (upper), and ribosome footprints on
846 *CCW22* uORF at high (V and11h) and low TE (T0) stages (lower). The ribosome footprint reads
847 were normalized similarly as in Fig. 2G (lower panel).
848 (H) Data-directed structure model of *CCW22* mRNA, shown as an arc plot of base-pairing
849 probabilities.
850 (I) Western blot analysis of Ccw22p expressed from wild-type (top), structure-disrupted (middle),
851 and structure-restored (bottom) vectors. The red box indicates nucleotides mutated for structural
852 disruption. The blue box indicates nucleotides mutated to restore the 5′-end base pairing with the
853 3′UTR. The purple boxes indicate the start codon and stop codon of a *CCW22* uORF. Note that
854 the compensatory mutations in the 5′UTR also alter the Kozak sequence. While an oscillatory
855 expression pattern is restored, the Ccw22p expression strength could be affected.

Figure 4. mRNA unwinding power coordinates meiotic proteostasis

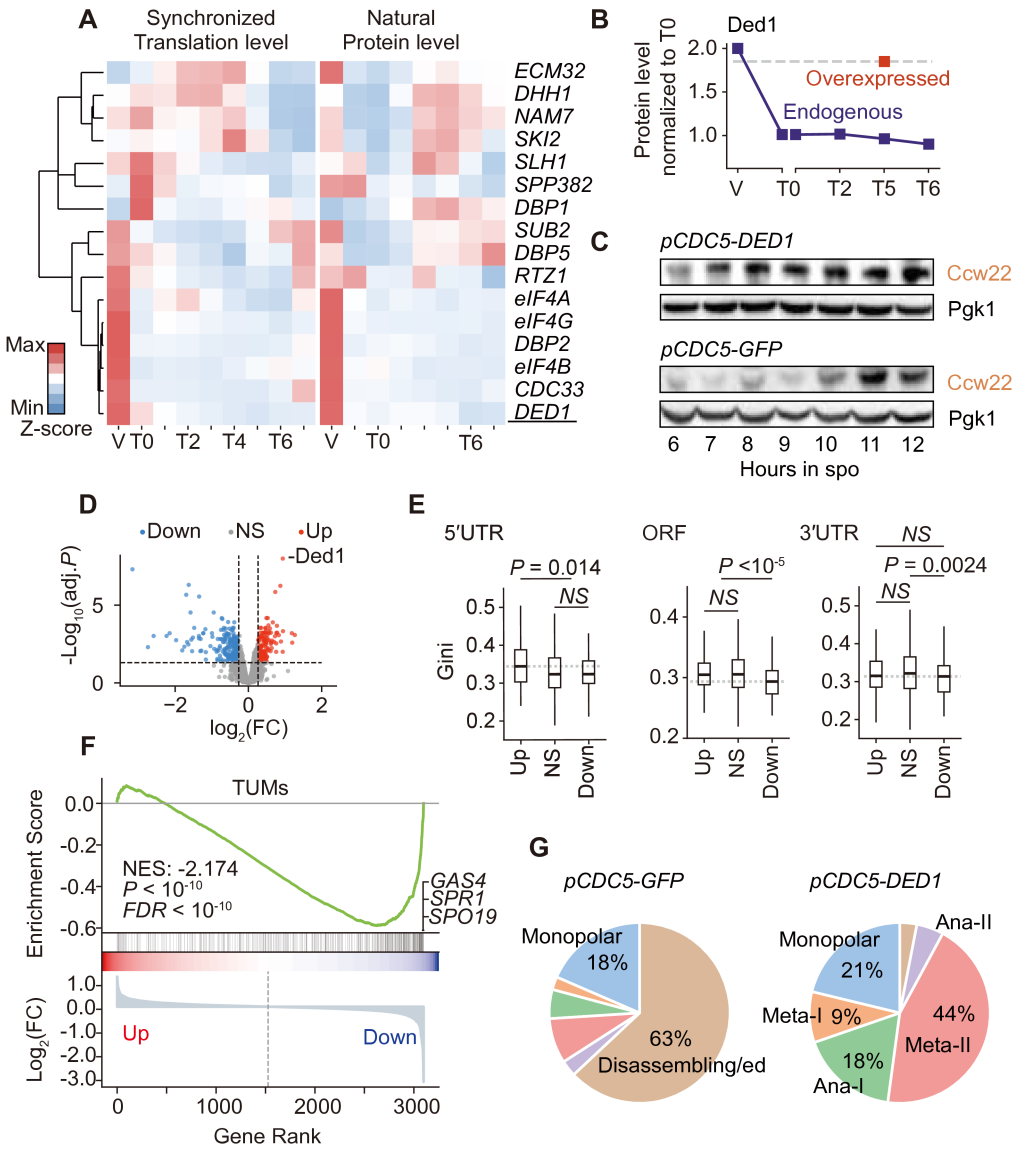

(A) Co-hierarchical clustering of 14 cytoplasmic RNA helicases and 2 accessory proteins during meiosis. Ribosome profiling data (left) were from synchronized meiosis, and proteomic data (right) were from strain undergoing natural meiosis.

(B) Endogenous Ded1p protein levels (blue squares) and overexpressed Ded1p protein level (red squares) at T5 stage driven by the *CDC5* promoter.

(C) Western blot analysis of Ccw22 expression in strains with Ded1p or GFP overexpression, both under the control of the *CDC5* promoter.

(D) Volcano plot of genes differentially expressed under Ded1 overexpression, with fold change (FC) > 1.2 and P < 0.05. Upregulated, n = 149; Downregulated, n = 194; Not significant, n = 2,761.

(E) Comparison of Gini indices across 5′UTR, ORF, and 3′UTR regions between differentially expressed genes under Ded1 overexpression.

(F) Gene Set Enrichment Analysis of TUMs protein level changes under Ded1 overexpression.

(G) Cell percentage of different meiotic stages at 12 hours post-induction in yeast strains overexpressing GFP or Ded1p.

872 **Figure 5. RNA structure and mRNA unwinding power orchestrate stage-**

873 **specific translation**

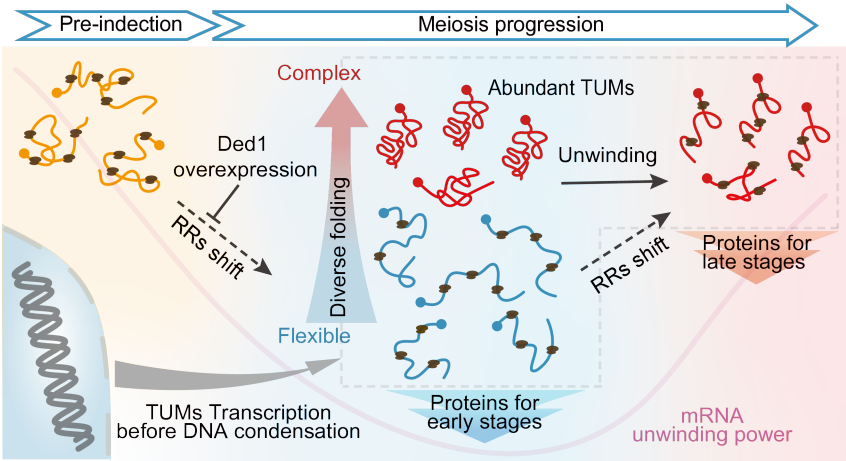

874

875 Model for how diverse RNA structures, coupled with oscillating mRNA unwinding power,
876 synergistically orchestrate the dynamic allocation of ribosome resources (RRs). These combined
877 features enable selective translation and precise protein synthesis during meiosis.

SUPPLEMENTAL FIGURE TITLES AND LEGENDS

Figure S1. Timepoint staging and DMS-MaP data quality control, related to Figure 1

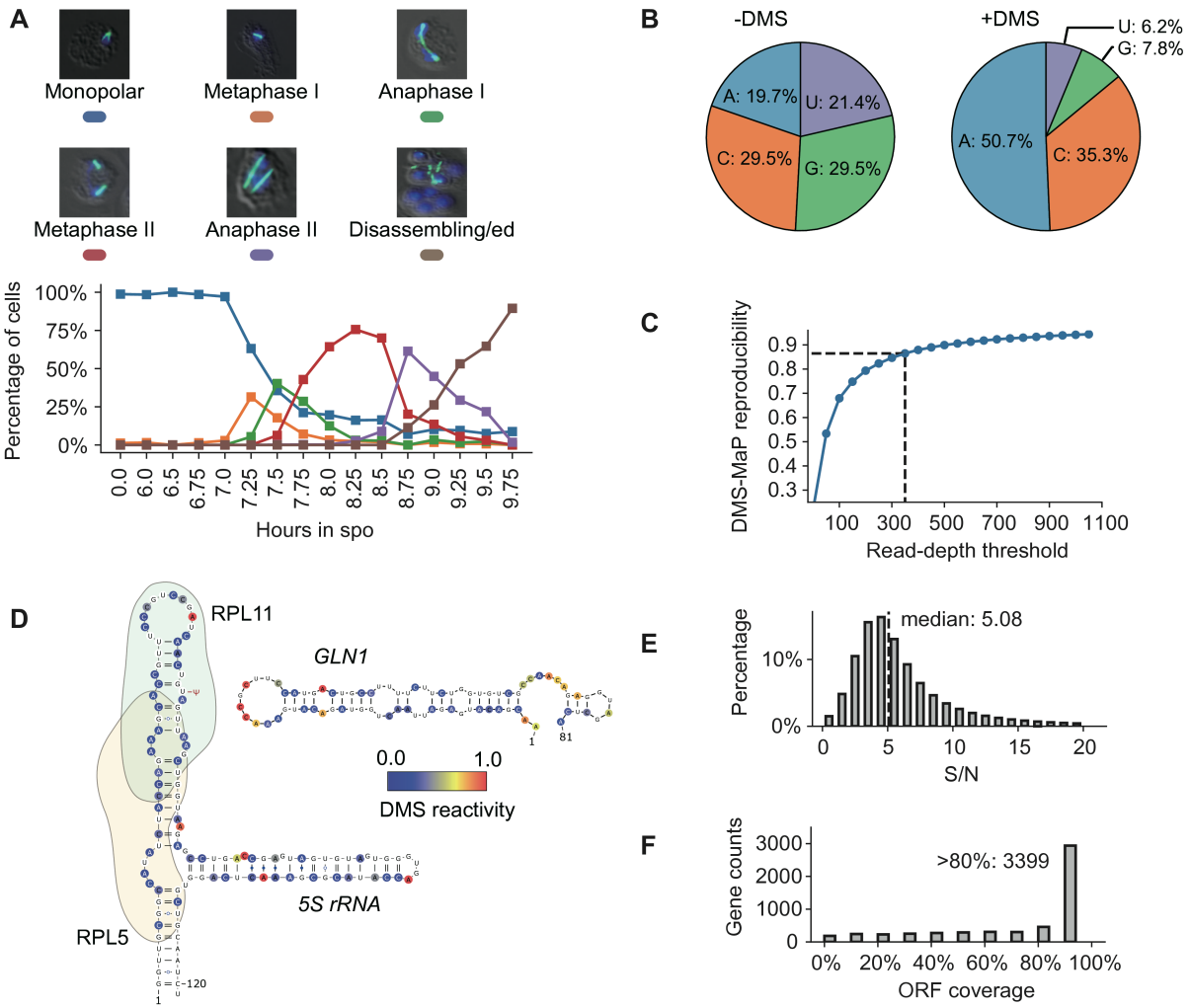

(A) Spindle morphologies corresponding to different stages (upper; blue, DAPI; green, anti-tubulin), and the cell percentages of different stages at sampled time points in synchronous meiosis (lower).
(B) Mutation rates of four nucleotides as detected by DMS-MaP. '+DMS' denotes libraries treated with DMS, and '-DMS' represents control libraries treated with DMSO.
(C) Pearson correlation coefficients of DMS reactivity between two replicates at various read-depth thresholds. The dotted line marks the correlation at a 350× read-depth threshold.
(D) Data-directed *in vivo* structural model of 5S rRNA, highlighting the binding sites for ribosomal proteins RPL5 and RPL11.
(E) Distribution of signal-to-noise ratios in DMS reactivity data for nucleotides with read-depths greater than 350.
(F) Distribution of ORF coverage for genes with resolved overall structures.

Figure S2. Relationship between mRNA structural complexity and translation efficiency during meiosis, related to Figure 2

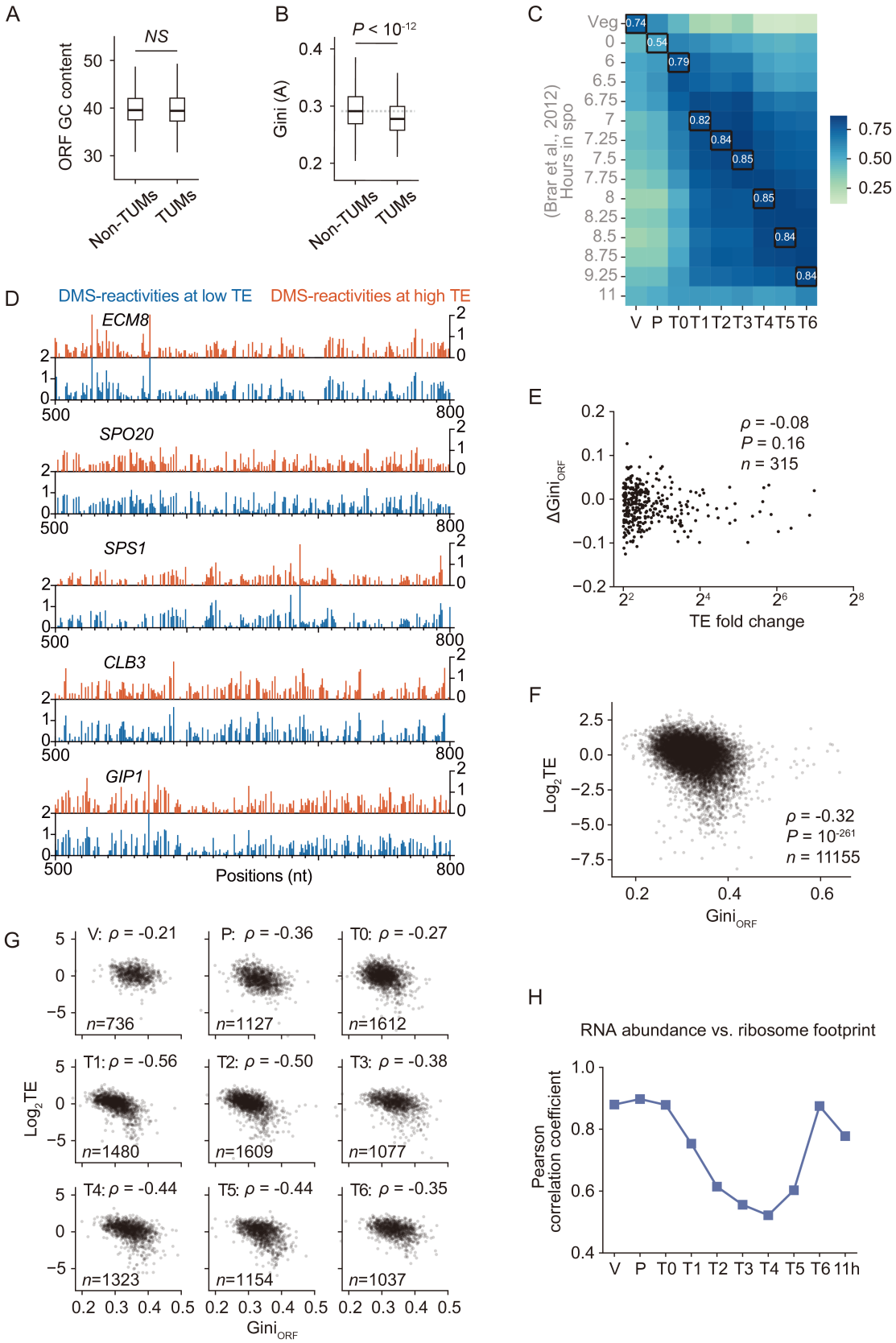

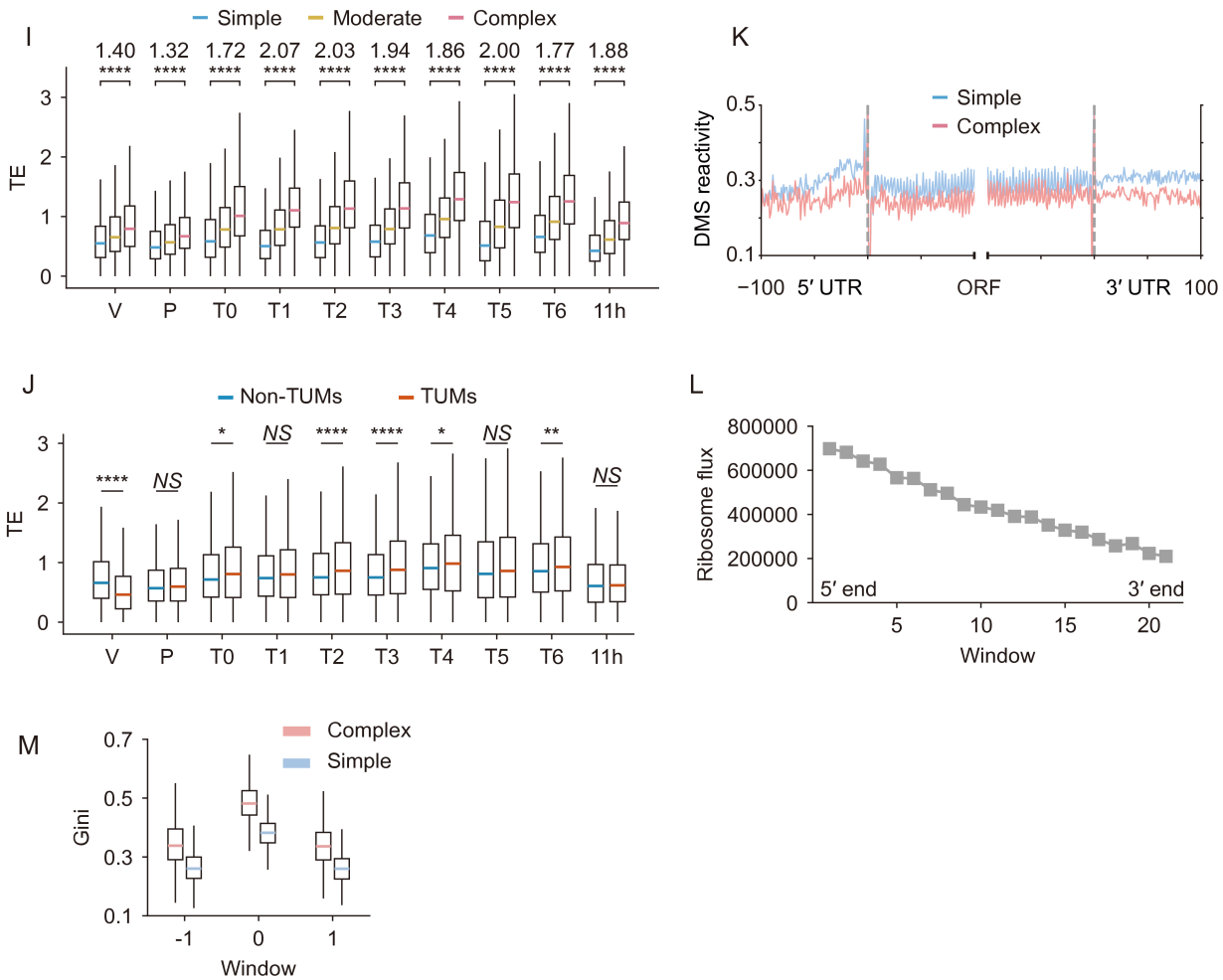

(A) Comparison of GC content between TUMs and non-TUMs.
(B) Comparison of Gini indices measured using a single kind of nucleotide (A) between TUMs and non-TUMs.
(C) Alignment of sampling time points with the ribosome profiling dataset[15] through RNA-seq profiles.
(D) Comparison of DMS reactivities within 300-nucleotide coding regions of five transcripts that have high or low TEs depending on meiotic stages. Fold changes in TE: *ECM8*, 106-fold; *SPO20*, 41-fold; *SPS1*, 25-fold; *CLB3*, 20-fold; *GIP1*, 15-fold.
(E) Relationship between changes in TEs and ORF Gini indices for transcripts with a TE fold change greater than 4.
(F) Spearman correlation analysis between TEs and ORF Gini indices across all time points.
(G) Spearman correlation analysis between TEs and ORF Gini indices at matched time points, related to Fig. 2D.
(H) Pearson correlation analysis between mRNA abundance and ribosome profiling data across all time points.
(I) Distribution of TEs for mRNA groups with different structural complexities across meiosis.
(J) Distribution of TEs for TUMs and non-TUMs across meiosis.
(K) Meta-gene analysis of DMS reactivities in Simple and Complex mRNA groups.
(L) Ribosome flux from the 1st to the 20th windows from the 5′ end to the 3′ end of mRNA ORF regions, related to Fig. 2F.
(M) Gini indices of the windows with the highest Gini index and their adjacent windows in Simple and Complex mRNA groups, related to Fig. 2F.

Figure S3. RNA structure-related temporal regulation of translation during meiosis, related to Figure 3

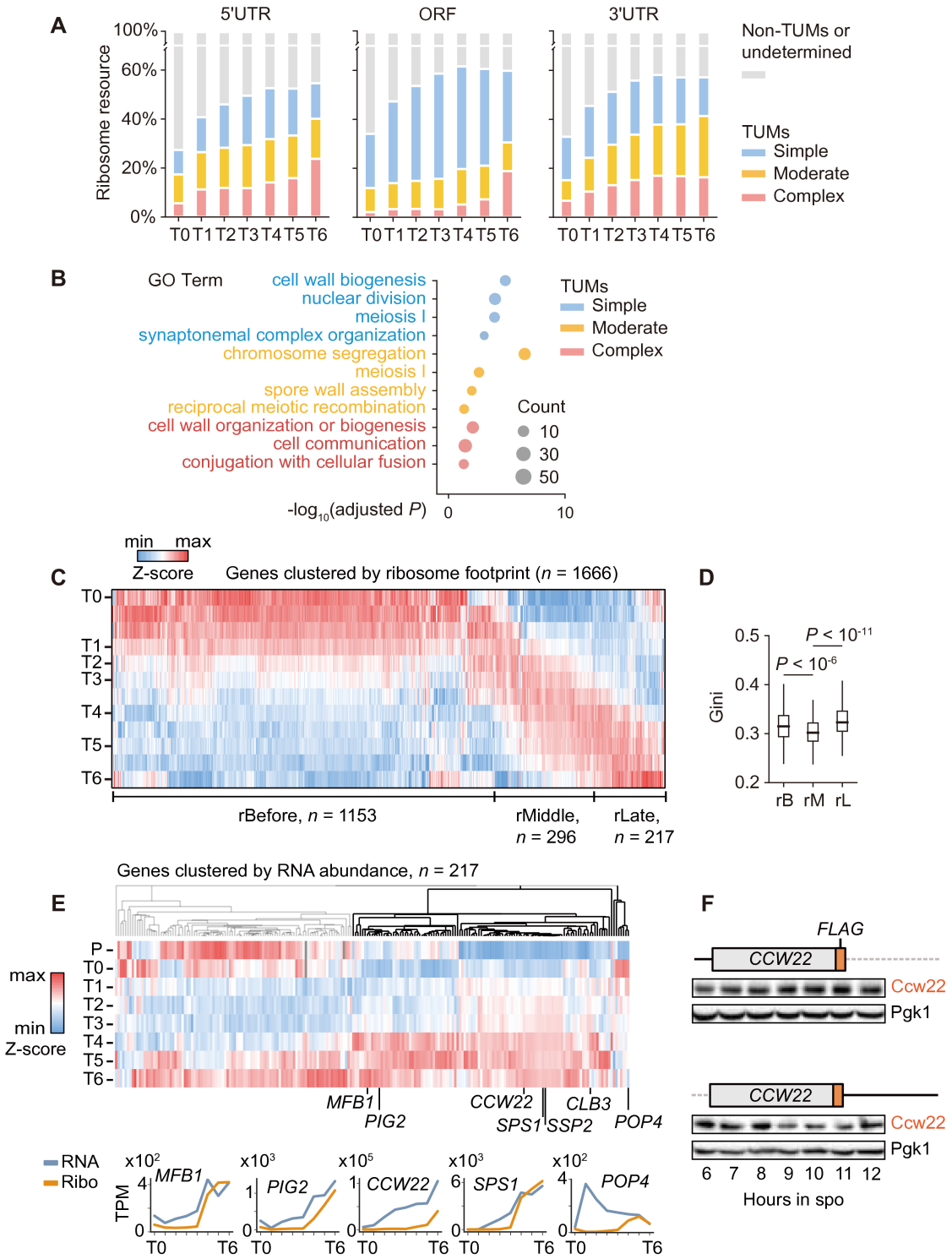

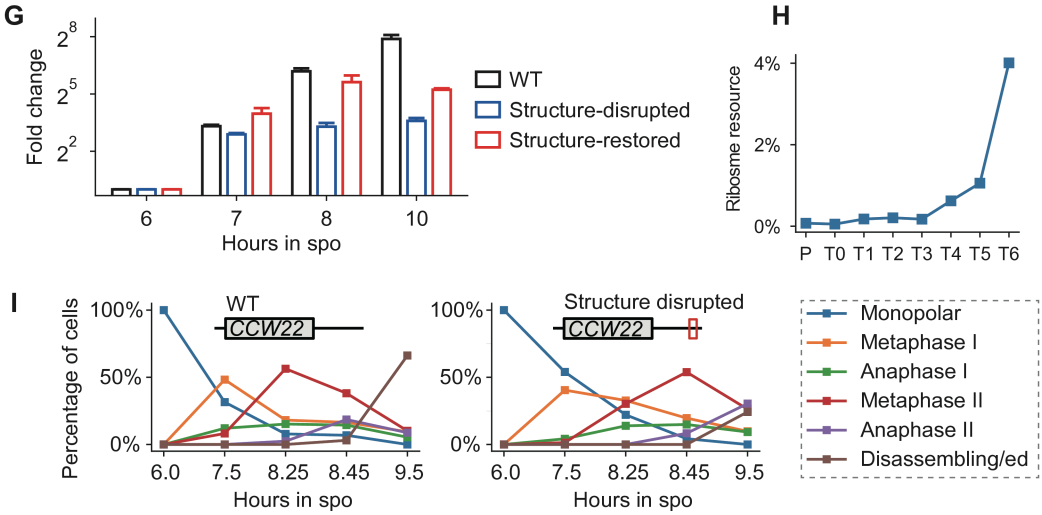

(A) Dynamic patterns of ribosome resource allocation among mRNA groups classified based on structural complexities in 5′UTR, ORF, and 3′UTR regions, related to Fig. 3A

(B) Gene Ontology enrichment analysis of three mRNA groups with different structural complexities, related to Fig. 3A.

(C) Hierarchical clustering of ribosome footprint for genes (n = 1,666) exhibiting more than an 8-fold change ($P < 0.05$) in TPM across meiosis, related to Fig. 3E.

(D) Comparison of Gini indices among three ribosome profiling groups: before meiosis (rBefore, n = 930); during mid-meiosis (rMiddle, n = 268), and near meiotic exit (rLate, n = 188).

(E) Hierarchical clustering of RNA abundance profiles (TPM) for genes in the rLate group. Line charts display RNA abundance and ribosome footprint throughout meiosis for five genes.

(F) Western blot analysis showing Ccw22p expression in a yeast strain harboring a 3′UTR or 5′UTR truncation vector.

(G) RNA abundance of *CCW22* mRNA, quantified by RT-qPCR, from wild-type, structure-disrupted, and structure-restored vectors, related to Fig. 3I.

(H) Ribosome resource allocation to *CCW22* mRNA across meiosis.

(I) Percentage of cells at each meiotic stage in yeast strains harboring wild-type or structure disrupted *CCW22* vectors.

943 **Figure S4. Oscillating pattern of RNA helicases and Ded1p overexpression**

944 **assay, related to Figure 4**

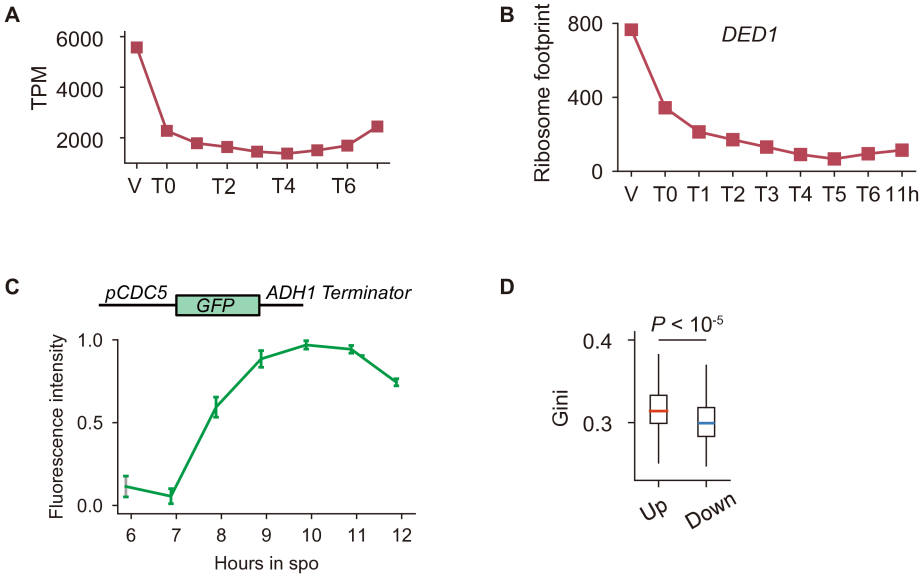

945

946 (A) Total ribosome footprint reads of RNA helicases, related to Fig. 4A.
947 (B) Ribosome footprint for *DED1* across meiosis.
948 (C) GFP intensity driven by the *CDC5* promoter.
949 (D) Comparison of Gini indices for upregulated and downregulated genes under Ded1p
950 overexpression.

951 # Supplemental information

952 Table S1. DMS-MaP sequencing depth for each stage.
953 Table S2. Quantitative data including RNA abundance, RNA structural complexity, matched
954 ribosome footprint, and protein abundance across meiosis.
955 Table S3. Statistics of stage-specific structures.
956 Table S4. Gene Ontology Enrichment Analysis results, related to Fig. S3B.
957 Table S5. Publication enrichment from the Saccharomyces Genome Database.
958 Table S6. The classification by structural complexity of transcripts with early and delayed
959 translation timing, related to Fig. S3C and S3D.
960 Table S7. Structure complexity of 5′UTR, ORF, and 3′UTR regions, related to Fig. 3E, 4E and
961 S3A.
962 Table S8. RNA helicase expression at translation and protein levels, related to Fig. 4A, 4B and
963 S4A.
964 Table S9. Differential gene expression analysis upon Ded1 overexpression, related to Figure 4D
965 and 4F.